CANCER

NK cells with tissue-resident traits shape response to immunotherapy by inducing adaptive antitumor immunity

Nicole Kirchhammer[1]*†, Marcel P. Trefny[1]‡, Marina Natoli[1]‡, Dominik Brücher[2]†‡, Sheena N. Smith[2]†, Franziska Werner[1]§, Victoria Koch[1], David Schreiner[3], Ewelina Bartoszek[4], Mélanie Buchi[1], Markus Schmid[2]||, Daniel Breu[2]¶, K. Patricia Hartmann[2], Polina Zaytseva[2]#, Daniela S. Thommen[5], Heinz Läubli[6], Jan P. Böttcher[7], Michal A. Stanczak[1]**, Abhishek S. Kashyap[1]††, Andreas Plückthun[2], Alfred Zippelius[1,6]*

T cell–directed cancer immunotherapy often fails to generate lasting tumor control. Harnessing additional effectors of the immune response against tumors may strengthen the clinical benefit of immunotherapies. Here, we demonstrate that therapeutic targeting of the interferon-γ (IFN-γ)–interleukin-12 (IL-12) pathway relies on the ability of a population of natural killer (NK) cells with tissue-resident traits to orchestrate an antitumor microenvironment. In particular, we used an engineered adenoviral platform as a tool for intratumoral IL-12 immunotherapy (AdV5–IL-12) to generate adaptive antitumor immunity. Mechanistically, we demonstrate that AdV5–IL-12 is capable of inducing the expression of CC-chemokine ligand 5 (CCL5) in CD49a$^+$ NK cells both in tumor mouse models and tumor specimens from patients with cancer. AdV5–IL-12 imposed CCL5-induced type I conventional dendritic cell (cDC1) infiltration and thus increased DC-CD8 T cell interactions. A similar observation was made for other IFN-γ–inducing therapies such as Programmed cell death 1 (PD-1) blockade. Conversely, failure to respond to IL-12 and PD-1 blockade in tumor models with low CD49a$^+$ CXCR6$^+$ NK cell infiltration could be overcome by intratumoral delivery of CCL5. Thus, therapeutic efficacy depends on the abundance of NK cells with tissue-resident traits and, specifically, their capacity to produce the DC chemoattractant CCL5. Our findings reveal a barrier for T cell–focused therapies and offer mechanistic insights into how T cell–NK cell–DC cross-talk can be enhanced to promote antitumor immunity and overcome resistance.

INTRODUCTION

The clinical success of immune checkpoint blockade has initially kept the scientific focus predominantly on factors regulating T cell activity (*1*). It is, however, increasingly acknowledged that a diverse range of immune cells, including components of innate immunity, must function in a coordinated and synergistic manner to successfully achieve immune-mediated tumor rejection (*2*–*4*).

The interferon-γ (IFN-γ)–interleukin-12 (IL-12) axis plays a central role in connecting innate and adaptive cancer immunity (*5*). Mainly produced by dendritic cells (DCs) in the tumor microenvironment, IL-12 stimulates cytotoxicity and cytokine secretion in T cells and natural killer cells (NK cells) (*6*). In a positive IL-12–IFN-γ feedback loop, T cell– and NK cell–derived IFN-γ, in turn, activates and induces IL-12 expression in DCs. Moreover, IFN-γ enhances antigen cross-presentation by antigen-presenting cells, thereby further potentiating the cytotoxic activity of CD8 T cells (*5*, *7*). Consequently, gene expression signatures reflecting cellular components of this axis—NK cells, DCs, and CD8 T cells—as well as signatures of IFN-γ signaling are predictive of improved patient survival in multiple cancer types (*8*–*12*). Furthermore, it has been shown that IL-12 induction by IFN-γ is essential for the efficacy of immune checkpoint blockade (*5*).

IL-12 has been extensively investigated for its use in cancer immunotherapy and has demonstrated remarkable antitumor efficacy in tumor models. However, in early clinical trials, its therapeutic benefit in patients remained limited with severe dose-limiting toxicity (*13*, *14*). A possible explanation is a lack of targeting to the tumor microenvironment. Most cytokines, including IL-12, act locally in the tumor and nearby lymph nodes in a paracrine or autocrine fashion, rather than systemically (*15*). Although multiple approaches using localized IL-12 delivery are currently under investigation, the antitumor efficacy of local IL-12 therapy observed in mice has yet to be replicated in humans (*16*–*19*).

[1]Cancer Immunology, Department of Biomedicine, University of Basel and University Hospital Basel, 4031 Basel, Switzerland. [2]Department of Biochemistry, University of Zurich, 8057 Zurich, Switzerland. [3]Immune Cell Biology, Department of Biomedicine, University Hospital Basel, 4031 Basel, Switzerland. [4]Microscopy Core Facility, Department of Biomedicine, University Hospital Basel, 4031 Basel, Switzerland. [5]Division of Molecular Oncology and Immunology, Netherlands Cancer Institute, 1066 Amsterdam, Netherlands. [6]Medical Oncology, University Hospital Basel, 4031 Basel, Switzerland. [7]Institute of Molecular Immunology and Experimental Oncology, Klinikum Rechts der Isar, School of Medicine, Technical University of Munich (TUM), 81675 Munich, Germany.
*Corresponding author. Email: nicole.kirchhammer@unibas.ch (N.K.); alfred.zippelius@usb.ch (A.Z.)
†Present address: Vector BioPharma AG, 4051 Basel, Switzerland.
‡These authors contributed equally to this work.
§Present address: Molecular Dermato-Oncology and Tumor Immunology, Department of Dermatology, General Hospital Vienna, 1090 Vienna, Austria.
||Present address: Roche Diagnostics GmbH, 82377 Penzberg, Germany.
¶Present address: Department of Immunology, University Hospital Zurich, 8091 Zurich, Switzerland.
#Present address: Institute for Regenerative Medicine, University of Zurich, 8952 Schlieren, Switzerland.
**Present address: Bloomberg-Kimmel Institute for Cancer Immunotherapy and Department of Oncology, Johns Hopkins University School of Medicine, Baltimore, MD 21287, USA.
††Present address: Boehringer Ingelheim Pharmaceuticals Inc., Ridgefield, CT 06877, USA.

Kirchhammer *et al.*, *Sci. Transl. Med.* **14**, eabm9043 (2022)   13 July 2022

1 of 17

Here, we sought to gain a deeper understanding of how IL-12–mediated tumor control is achieved and whether this knowledge ultimately allows to design improved treatment strategies for efficient tumor control. To this end, we used a tumor-targeted adenovirus serotype 5 delivery platform as a tool for intratumoral IL-12 immunotherapy (AdV5–IL-12) (20–22). In tumor models and patient-derived model systems, we demonstrate that the efficacy of IL-12 depends on the intratumoral abundance of a population of CD49a^{+} NK cells with tissue-resident traits and their ability to prime the immune microenvironment by producing the chemokine CCL5. In CD49a^{+} CXCR6^{+} NK cell[poor] tumors, resistance to IL-12 can be rescued by induced expression of CCL5, leading to increased infiltration of type I conventional DCs (cDC1s), which then set the positive antitumor DC–T cell feedback loop in motion. Similarly, resistance to other IFN-γ–mediated treatments such as PD-1 checkpoint blockade can be a result of reduced CCL5 induction due to a lack of CD49a^{+} CXCR6^{+} NK cells and can be overcome by treatment with CCL5. Our data highlight the importance of NK cells with tissue-resident traits for the induction of DC–T cell cross-talk and successful cancer immunotherapy.

RESULTS

IL-12 immunotherapy prompts NK cells to orchestrate an antitumor microenvironment

Although strategies to maximize IL-12 delivery are of increasing clinical interest, the therapeutic benefit in patients remains moderate. We first sought to identify cell types and key pathways underlying successful clinical outcomes to intratumoral IL-12 therapy in patients with melanoma (IL-12MEL trial; NCT01502293) (16). To this end, we correlated tumor immune signatures derived from pretreatment tumor biopsies with therapeutic responses. Patients with clinical responses showed higher NK cell and CD8 T cell scores compared to patients with tumor progression, whereas no correlation was found with the scores of other immune cells (Fig. 1A and fig. S1A).

To define a model system for local IL-12 therapy that reflects these clinical findings, we used a nonreplicative, shielded, and retargeted AdV5 vector previously established in our laboratory (20–22). For this study, human epidermal growth factor receptor 2 (HER2) was used as a model antigen to target the HER2-overexpressing syngeneic tumor cell lines B16-HER2 and EMT6-HER2. Because of the high abundance of preexisting antibodies against AdV5 in humans, we made use of a shield based on a hexon-binding humanized single-chain variable fragment, fully covering the virion (22). To confirm the tumor-specific expression of our payload, luciferase-encoding virus (AdV5-Luc) was peritumorally injected into B16-HER2– and EMT6-HER2–bearing mice (fig. S1B). In both tumor models, the payload was exclusively expressed in the tumor for up to 10 days with a peak expression on day 1 (fig. S1, C to E).

To evaluate the efficacy of AdV5-IL12, we peritumorally treated mice bearing orthotopic (intramammary) EMT6-HER2 tumors with four injections of 1.5×10^8 plaque-forming units (PFU) of retargeted and shielded AdV5–IL-12 initiated at day 7 after tumor inoculation. Empty virus (AdV5-control) served as a control (Fig. 1B). Treatment with AdV5–IL-12 resulted in inhibition of tumor growth, enhanced survival, and complete tumor regression in 70% of treated mice; AdV5-control showed only moderate effects (Fig. 1, C and D). No IL-12 was detected in the serum, confirming the specificity of our tumor-localized therapy (fig. S1F). Retargeted and shielded AdV5–IL-12 showed increased efficacy compared to naked and retargeted vectors (fig. S1G).

As patients with localized IL-12 therapy show clinical responses even in nontreated lesions, we assessed the systemic effects of AdV5–IL-12 in our mouse tumor model. To this end, we injected HER2-negative EMT6 wild-type (WT) cells into the contralateral flanks of the EMT6-HER2 tumor–bearing mice (fig. S1H). We observed a reduced tumor growth of the contralateral tumors and complete regression in 50% of the AdV5–IL-12–treated animals. This indicates systemic immune effects upon local administration of AdV5-IL12.

AdV5–IL-12 induced the formation of protective antitumor immunological memory, because mice that survived primary EMT6-HER2 engraftment after AdV5–IL-12 treatment remained tumor-free after later rechallenge with the same cell line 80 days after the first tumor cell inoculation (fig. S1I). Tumors from mice simultaneously inoculated with EMT6 WT cells on the lateral flank were equally rejected, suggesting broad memory formation against shared antigens expressed by EMT6 cells (fig. S1I).

To dissect the role of defined immune cell populations in mediating the therapeutic effect of AdV5–IL-12, we performed antibody-mediated depletion studies (Fig. 1E). In agreement with the immune signature analysis from the IL-12MEL trial (Fig. 1A), AdV5–IL-12 required both CD8 T cells and NK cells for therapeutic efficacy. Because IL-12 is a known driver of IFN-γ production in both those cell types and the clinical response correlates with a defined IFN-γ score (16), we assessed the contribution of IFN-γ to the activity of AdV5–IL-12. IFN-γ–neutralized mice failed to control EMT6-HER2 tumors upon treatment with AdV5-IL12 (fig. S1J). In line with these findings, AdV5–IL-12 increased the capacity of CD8 T cells and NK cells to proliferate and to exert effector functions, as assessed by flow cytometry (figs. S2 and S3). In conclusion, mirroring the clinical situation, AdV5–IL-12 treatment in EMT6-HER2 tumors requires robust NK and CD8 T cell responses, which depend on IFN-γ.

We next assessed the capability of CD8 and NK cells to directly interact and attack cancer cells using a highly multiplexed cytometric imaging approach, termed co-detection by indexing (CODEX) (23). AdV5–IL-12 led to a pronounced accumulation of CD45^{+} immune cells (fig. S4, A and B). Spatial proximity (defined as a distance of <50 μm) of NK and CD8 T cells with tumor cells was specifically increased upon AdV5–IL-12 treatment (Fig. 1F and fig. S4C). To confirm functional interactions and tumor lysis by NK and CD8 T cells, we analyzed the expression of the effector marker granzyme B (GzmB) in cells with spatial proximity to tumor cells (CD45^{−} CD31^{−}). In both NK and CD8 T cells, the number of GzmB^{+} cells was increased in close proximity to tumor cells (Fig. 1G). In addition, the spatial proximity of CD8 T cells with DCs was specifically enhanced after AdV5–IL-12 treatment (Fig. 1F). Moreover, the costimulatory molecules CD40, CD80, and major histocompatibility complex class II (MHCII), as well as programmed death-ligand 1 (PD-L1) on DCs in close proximity to CD8 T cells were specifically increased after AdV5–IL-12 treatment, indicating an enhanced functional interaction between DCs and CD8 T cells induced by IL-12 (Fig. 1H). We also noticed a close proximity of CD8 and NK to endothelial cells after AdV5–IL-12 treatment (Fig. 1, F and I), which may indicate induced trafficking of these cells by IL-12.

To investigate IL-12–induced immune cell recruitment to the tumor, we blocked lymphocyte recirculation with the trafficking

Fig. 1. IL-12 immunotherapy prompts NK cells to orchestrate an antitumor microenvironment. (**A**) Cell signature scores measured by NanoString in skin tumor biopsies from 19 patients with melanoma before intratumoral treatment with ImmunoPulse IL-12 were correlated with clinical response (PD, progressive disease; SD, stable disease; PR, partial response) (16). (**B**) Wild-type (WT) mice were engrafted with 1×10^6 EMT6-HER2 intramammarily (i.m.). From day 7 (tumor size of 30 to 70 mm³), mice were treated with 1.5×10^8 PFU of HER2-targeted and HER-shielded adenoviral vectors [peritumorally (p.t.)] encoding for IL-12 or an empty control cassette (AdV5-control) on days 7, 9, 11, and 14 peritumorally indicated by black arrows. (**C**) Tumor growth and (**D**) Kaplan-Meier survival curves are shown with the number of mice indicated. Black arrows denote days of treatment. Pooled data from at least three independent experiments. (**E**) For depletion studies, mice were injected intraperitoneally (i.p.) with anti-CD8 and anti-AsialoGM1 starting 1 day before adenoviral treatment. Tumor growth curves after depletion are shown. Black arrows denote days of adenoviral treatment. Pooled data from two independent experiments. $n = 6$ to 12 mice. (**F**) Visualization of odds ratios and $-\log_{10}(P$ values) for changes in cell-cell type interactions between experimental conditions focusing on interaction including CD8 T cells and NK cells. $n = 3$ mice per condition. Each one section was acquired. $N = 1$. (**G**) Representative immunofluorescence (IF) pictures are showing AdV5–IL-12–treated tumors (CD45, red; MHCI, blue; CD8, yellow; NKp46, green). White arrows are showing CD8 T cells (CD45⁺, MHCI⁺, and CD8⁺) or NK cells (CD45⁺, MHCI⁺, and NKp46⁺) neighboring tumor cells (CD45⁻ and MHCI⁺). Quantification of GzmB⁺ CD8 T cells and NK cells in close proximity (<50 μm) to tumor cells in comparison to more distant (>50 μm) proximity. Each dot represents the count in one acquired tumor. Treatment conditions were pooled in this analysis. $N = 1$. (**H**) Representative IF pictures are showing AdV5–IL-12–treated tumors (MHCII, red; CD11c, blue; CD8, yellow). White arrows are showing CD8 T cells (CD45⁺ and CD8⁺) neighboring DCs (CD45⁺, CD11c⁺, and F4/80⁻). Ratio of CD40, CD80, MHCII, and PD-L1 expression on the DC cluster in close (<50 μm) or distant (>50 μm) proximity to the CD8 T cell cluster comparing untreated and AdV5–IL-12–treated tumors is shown. (**I**) Representative IF pictures showing CD8 T cells and NK cells in close proximity to blood vessels in AdV5–IL-12–treated tumors (CD31, red; CD8, blue; NKp46, green). $n = 3$ mice per group. (**J**) EMT6-HER2–bearing mice were treated with AdV5–IL-12. NK cells were depleted using anti-AsialoGM1 antibody (intraperitoneally) as indicated (blue arrow). Tumors were isolated, and single-cell suspensions of tumor digest were analyzed using flow cytometry on day 16. $N = 1$. (**K**) Intratumoral cDC1s (CD11c⁺, F4/80⁻, Ly-6G⁻, MHCII⁺, CD103⁺, and CD11b^low) were quantified after AdV5–IL-12 treatment ± NK depletion. (**L**) Mean fluorescence intensity (MFI) of GzmB on CD8 T cells (CD3⁺, CD8⁺, NKp46⁻, CD19⁻, and Ly-6G⁻). (**M**) Polarization of macrophages (CD11b⁺ F4/80⁺) after AdV5–IL-12 treatment comparing NK depletion versus nondepleted. (K to M) $n = 4$ to 5 mice per group. *$P < 0.05$, **$P < 0.01$, ***$P < 0.001$, and ****$P < 0.0001$. Error bar values represent SD or SEM (tumor growth curves). For comparisons between three or more groups, one-way ANOVA with multiple comparisons was used. For survival analysis, P values were computed using the log rank test. Two-way ANOVA was used to compare tumor growth curves.

Kirchhammer *et al.*, *Sci. Transl. Med.* **14**, eabm9043 (2022)   13 July 2022

3 of 17
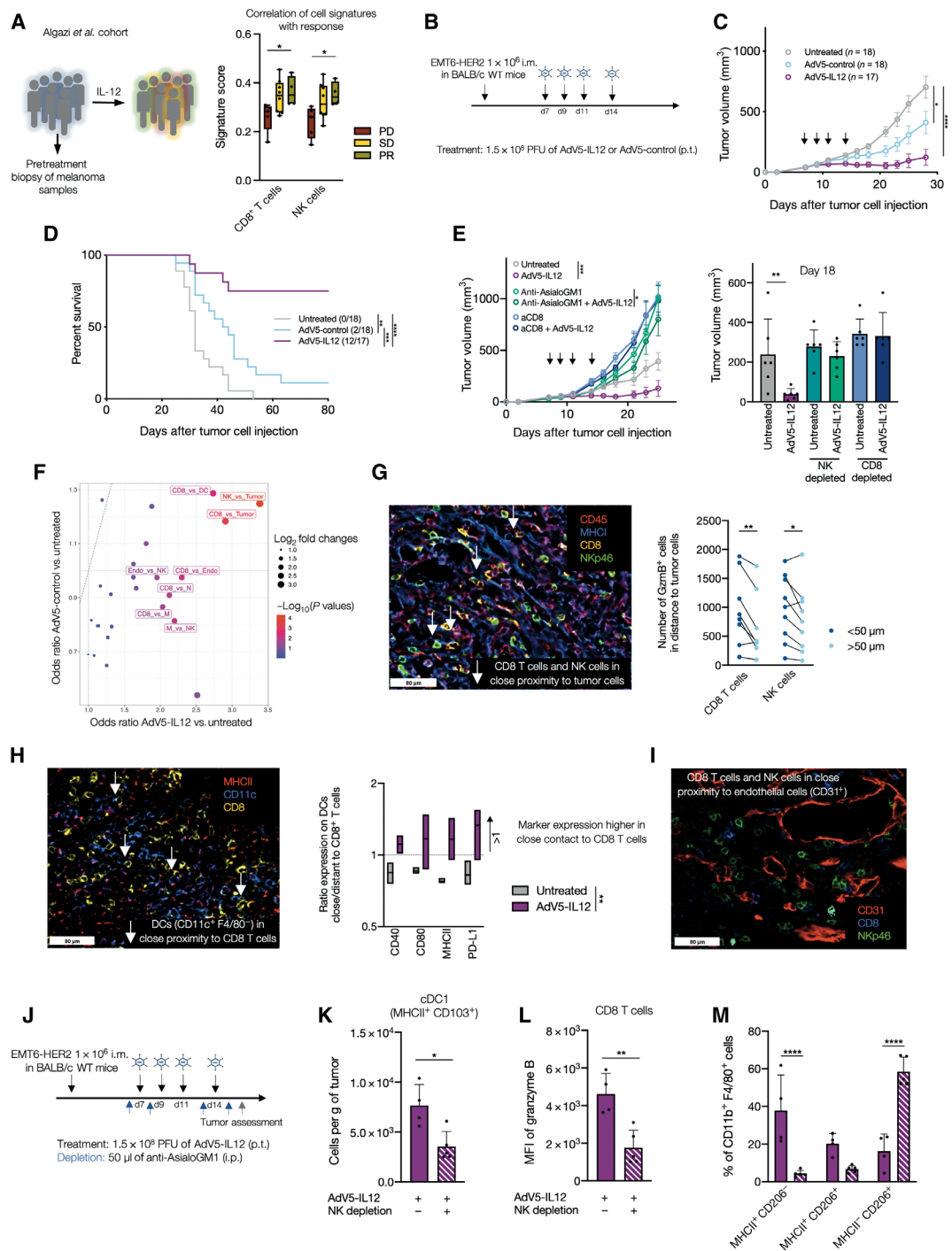
inhibitor FTY720 (24). FTY720 treatment before tumor inoculation fully abrogated tumor control. Blocking trafficking during AdV5–IL-12 treatment allowed initial tumor control but did not result in complete tumor regression (fig. S4D). This suggests that efficacious IL-12 responses require both preexisting and actively recruited tumor-infiltrating lymphocytes (TILs).

In addition to direct cytotoxicity against tumor cells, NK cells were shown to drive immune cell infiltration and intrinsic inflammation within tumors (2, 9). To dissect the impact of NK cells on IL-12–induced recruitment, we depleted NK cells throughout the AdV5–IL-12 treatment and assessed fate and infiltration of tumor-infiltrating immune cells (Fig. 1J and fig. S3). NK cell depletion led to a reduced number of MHCII$^+$ CD103$^+$ cDC1s (CD11c$^+$ F4/80$^-$; Fig. 1K). Furthermore, NK depletion was associated with reduced GzmB expression in CD8 T cells, suggesting an important role of NK cells in facilitating optimal antitumor CD8 T cell responses (Fig. 1L). The number of macrophages (CD11b$^+$ F4/80$^+$) in the tumor was unchanged; however, depletion of NK cells skewed the polarization toward an immunosuppressive M2 (CD206$^+$ MHCII$^-$) phenotype (Fig. 1M). Thus, we concluded that, during AdV5–IL-12 treatment, NK cells orchestrate the recruitment and priming of essential cell subsets, including cDC1s, and activate CD8 T cells to enhance tumor killing.

CCL5, mainly produced by CD49a$^+$ CXCR6$^+$ NK cells, is required for IL-12–mediated tumor rejection

To identify clinically relevant chemokines that may guide immune cell recruitment by NK cells after IL-12 therapy, we correlated NK cell scores with the expression of chemokines and their receptors in patients responding to IL-12 therapy (Fig. 2A). We identified that *CCL5* and its receptor *CCR5* strongly correlated with an NK score (Fig. 2B). Accordingly, *CCL5* was up-regulated in patients with clinical responses (Fig. 2C). These results suggest that NK cells, likely through CCL5, are important in facilitating clinical responses to IL-12.

We therefore investigated whether NK cell–mediated CCL5 contributes to the efficacy of AdV5–IL-12 in EMT6-HER2 tumors (intramammary). In line with the observed CCL5 upregulation in responding patients (Fig. 2C), AdV5–IL-12 treatment of EMT6-HER2 tumors induced CCL5 expression in tumor lysates (Fig. 2D). CCL5 concentrations were reduced in tumor lysates after NK cell depletion, which confirms that, in this model, NK cells are the main source of CCL5 induced by AdV5–IL-12 (Fig. 2D). Neutralizing CCL5 before tumor inoculation fully abrogated IL-12 efficacy; CCL5 neutralization after tumor inoculation but before AdV5–IL-12 treatment partially inhibited IL-12 efficacy (Fig. 2E). Therefore, we concluded that CCL5 produced by NK cells plays a dual role in the response to IL-12 delivery. CCL5 at the steady state permits responsiveness to AdV5–IL-12 treatment, and further induction of CCL5 by AdV5-IL12 treatment may attract immune cells to improve antitumor immunity.

To analyze the contribution of CCL5 to NK cell–mediated tumor rejection upon AdV5–IL-12 treatment, NK-depleted tumor-bearing mice were concomitantly treated with AdV5–IL-12 and an AdV5 encoding CCL5 (AdV5-CCL5). Although depletion of NK cells abrogated the efficacy of AdV5–IL-12, the combination of AdV5-CCL5 with AdV5–IL-12 partly rescued its efficacy (fig. S4E).

Recent studies have revealed that NK cells are highly heterogeneous with different immune functions (25–27). To identify which

NK cell subset produced CCL5, we analyzed CCL5 expression after AdV5–IL-12 treatment in subpopulations of NK cells reflecting different maturation stages and subtypes, defined by CD11b and CD27 expression and by markers associated with homing or tissue residency (28, 29). We observed a higher proportion of NK cells associated with tissue residency (CXCR6$^+$ and CD49a$^+$, CD11b$^-$), producing CCL5 compared to mature (CD11b$^+$) CXCR6- and CD49a-low conventional NK (cNK) cells (Fig. 2F). Those CCL5-producing NK cells were also characterized by a high expression of CD27 (nonmature) and CD69 (associated with tissue residency) and showed a low expression of CD62L, which facilitates homing to secondary lymphatic tissues (fig. S4F). These findings suggest that responsiveness to IL-12 depends on CCL5-producing NK cells, which exhibit features associated with tissue residency with low maturation profile.

AdV5-CCL5 overcomes AdV5–IL-12 resistance in CD49a$^+$ CXCR6$^+$ NK cell–poor tumors

Because CD49a$^+$ CXCR6$^+$ NK cell–derived CCL5 was associated with treatment efficacy, we hypothesized that tumors with a lower proportion of this NK cell subpopulation would be largely resistant to AdV5–IL-12 and could benefit from CCL5 supplementation. To test this and to exclude tumor cell–intrinsic resistance mechanisms, we injected EMT6-HER2 cells subcutaneously, where we observed a lower amount of CD49a$^+$ CXCR6$^+$ NK cells (Fig. 3A), whereas a similar number of cNK cells was assessed (Fig. 3B). Treatment of subcutaneous EMT6-HER2 tumors (CD49a$^+$ CXCR6$^+$ NK cell^{poor} tumor microenvironment) with AdV5–IL-12 did not lead to a substantial tumor reduction (fig. S5A), in contrast to intramammary-injected tumors (Fig. 1C and fig. S5B). However, we could observe an improved outcome when combining AdV5–IL-12 treatment with AdV5-CCL5 in this setting (fig. S5A), confirming our hypothesis that a lack of CD49a$^+$ CXCR6$^+$ NK cells can be at least partially rescued by CCL5 supplementation. To exclude a more general, NK cell–unrelated benefit of CCL5 supplementation, we treated mice bearing intramammary EMT6-HER2 tumor (CD49a$^+$ CXCR6$^+$ NK cell^{rich} tumor microenvironment) with the combination of both viral vectors, which did not lead to an improved tumor control (fig. S5B).

To strengthen our conclusion, we used subcutaneous B16-HER2 as an orthotopic tumor model, which showed not only a low proportion of CD49a$^+$ CXCR6$^+$ NK cells but also a similar number of cNK cells compared to the intramammary EMT6-HER2 model (Fig. 3, A and B). In line with our findings that CD49a$^+$ CXCR6$^+$ NK cells are the major source of CCL5, the amount of CCL5 was not increased after AdV5–IL-12 treatment in B16-HER2 tumors (Fig. 3C), in contrast to intramammary EMT6-HER2 tumors (Fig. 2D). Unlike in intramammary EMT6-HER2 tumors, NK cell depletion in B16-HER2 tumors did not increase the tumor growth of untreated or AdV5–IL-12–treated tumors, which supports our hypothesis that, mainly, NK cells with tissue-resident traits but not mature cNK cells determine IL-12 responsiveness (Figs. 1E and 3D).

We then asked whether therapeutic CCL5 delivery using AdV5-CCL5 may compensate for the lack of CD49a$^+$ CXCR6$^+$ NK cells when combined with AdV5–IL-12 in B16-HER2–bearing mice (Fig. 3E). The combination further increased survival compared to AdV5–IL-12 alone. We further confirmed our finding in mice bearing subcutaneous MC-38 tumors with low amounts of CD49a$^+$ CXCR6$^+$ NK cells comparable with B16-HER2 tumors (Fig. 3A). Therefore, we used shielded vectors without retargeting to allow intrinsic
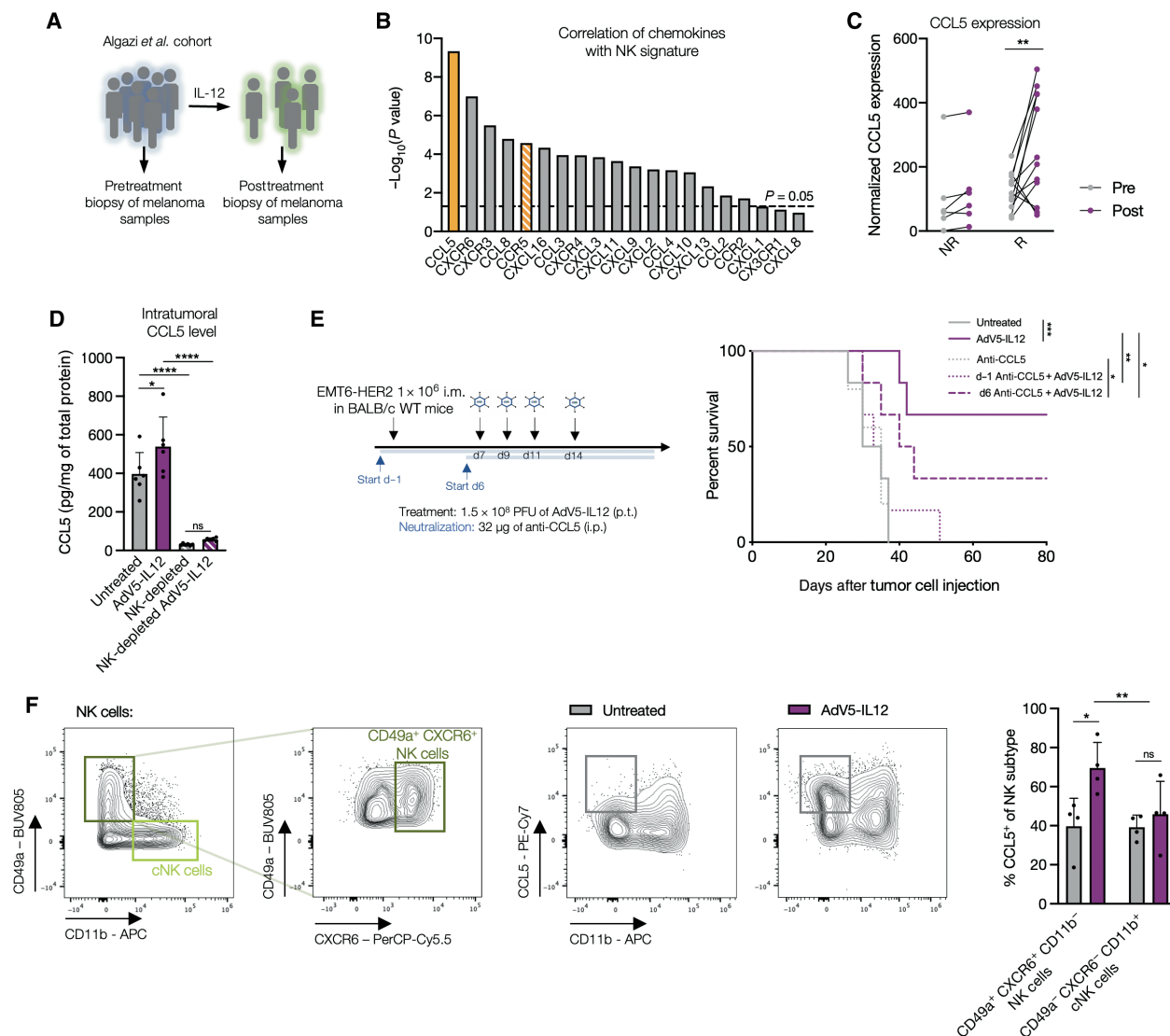
Kirchhammer *et al.*, *Sci. Transl. Med.* **14**, eabm9043 (2022)   13 July 2022

4 of 17

Fig. 2. CCL5, mainly produced by CD49a$^+$ CXCR6$^+$ NK cells, is required for IL-12–mediated tumor rejection. (**A**) NK cell signature scores measured by NanoString in skin tumor biopsies from responding patients with melanoma before intratumoral treatment with ImmunoPulse IL-12 were correlated with chemokines and their receptor. (**B**) −Log$_{10}$(P value) of chemokines and their receptors that are correlating with NK signature are shown. Values over dashed line are significant. (**C**) Normalized counts of *CCL5* expression of patients with no response (NR: PD) versus response (R: SD + PR) before and after intratumoral treatment with ImmunoPulse IL-12 determined by NanoString. (**D**) EMT6-HER2–engrafted mice (intramammary) were treated with AdV5–IL-12 and/or anti-AsialoGM1 antibody on days 7, 9, and 11 after tumor inoculation; tumors were isolated and lysed. CCL5 expression was determined by ELISA and normalized to total protein measured by bicinchoninic acid assay (BCA). n = 6 per condition. Two-tailed Student's t test was used. N = 1. (**E**) EMT6-HER2–engrafted mice were treated with AdV5–IL-12 after the indicated schedule, as shown by the black arrows. Starting 1 day before tumor inoculation or 1 day before adenoviral therapy, CCL5 was neutralized using antibodies every 3 to 4 days, as shown by the blue arrows. Kaplan-Meier survival curves are shown. n = 6. N = 1. (**F**) Mice were treated with AdV5–IL-12 on days 7, 9, and 11 after EMT6-HER2 inoculation. On day 12, tumors were isolated and CCL5 was analyzed on NK cell subsets (CD49a$^+$ CXCR6$^+$ CD11b$^-$ cells or CD49a$^-$ CXCR6$^-$ CD11b$^+$ cNK cells). N = 1. *P < 0.05, **P < 0.01, ***P < 0.001, and ****P < 0.0001. ns, not significant. Error bar values represent SD or SEM (tumor growth curves). For comparisons between three or more groups, one-way ANOVA with multiple comparisons was used. For survival analysis, P values were computed using the log rank test. Two-way ANOVA was used to compare tumor growth curves. APC, antigen-presenting cell. BUV805, Brilliant ultraviolet 805; PerCP-Cy5.5, Peridin-Chlorophyll-protein complex cyanine 5.5; PE-Cy7, Phycoerythrin-Cyanine 7.

transduction mechanisms. The combination of AdV5–IL-12 with AdV5-CCL5 led to full tumor rejection in 50% of treated mice. Mice treated with AdV5–IL-12 alone did not reject any tumors (fig. S5C).

To define factors that could explain the lack of efficacy of IL-12 in CD49a$^+$ CXCR6$^+$ NK cell^{poor} tumors, we compared which cell interactions were induced after IL-12 therapy in the B16-HER2 compared to the EMT6-HER2 mouse tumor model (Fig. 3F and fig.

S6, A and B). We observed two major differences in the changes to the interactome in B16-HER2 tumors. We noticed lower induction of NK-tumor and CD8 T-tumor cells and lower induction of DC-CD8 T cell interactions by IL12 in the CD49a$^+$ CXCR6$^+$ NK cell^{poor} tumor microenvironment. Thus, CD49a$^+$ CXCR6$^+$ NK cell^{poor} B16-HER2 tumors are characterized by a reduced tumor attack of effector cells and reduced induction of DC-CD8 T cell cross-talk

Fig. 3. AdV5-CCL5 overcomes AdV5–IL-12 resistance in in CD49a⁺ CXCR6⁺ NK cell^poor tumors. (**A**) The amount of intratumoral CD49a⁺ CXCR6⁺ NK cell tumor was determined in untreated EMT6-HER2 intramammary, EMT6-HER2 subcutaneous, B16-HER2 subcutaneous, and MC-38 subcutaneous tumors. $N = 1$. (**B**) The amount of intratumoral cNK cell tumor was determined in untreated EMT6-HER2 intramammary, EMT6-HER2 subcutaneous, B16-HER2 subcutaneous, and MC-38 subcutaneous tumors. $N = 1$. (**C**) B16-HER2–engrafted mice were treated with AdV5–IL-12 on days 11, 13, and 15 after tumor inoculation; tumors were isolated and lysed on day 16. CCL5 expression was determined by ELISA and normalized to total protein measured by BCA. $n = 6$ per condition. $N = 1$. (**D**) WT mice were engrafted with 1×10^6 EMT6-HER2 (intramammarily) or 0.5×10^6 B16-HER2 (subcutaneously). Mice were treated with AdV5–IL-12 on days 7, 9, 11, and 14 or days 11, 13, 15, and 18 (tumor size of 30 to 70 mm³), respectively. NK cells were depleted using anti-AsialoGM1 and anti-NK1.1 antibody every 4 to 5 days starting 1 day before adenoviral therapy. Tumor volume on day 25 after tumor inoculation is shown. $N = 1$. (**E**) Mice were treated with AdV5–IL-12 and AdV5-CCL5 on days 11, 13, 15, and 18 (tumor size of 30 to 70 mm³) after B16-HER2 inoculation, as indicated by the black arrows: Kaplan-Meier survival curves are shown. $n > 15$ mice

per condition. Pooled data from at least three independent experiments. (**F**) Mice were engrafted with 1×10^6 EMT6-HER2 (intramammarily) or 0.5×10^6 B16-HER2 (subcutaneously). Starting from day 7 or 11 (tumor size of 30 to 70 mm³), mice were treated with 1.5×10^8 PFU of HER2-targeted and HER-shielded adenoviral vectors (peritumorally) encoding for IL-12 on days 7 or 11, 9 or 13, and 11 or 15. On day 12 or 16 after inoculation, tumors were isolated, embedded in OCT, and analyzed by multiparameter IF microscopy. $N = 1$. Visualization of odds ratios and P values for changes in cell-cell type interactions between EMT6-HER2 and B16-HER2, focusing on interaction including CD8 T cells and NK cells. (**G**) Mice were engrafted with 0.5×10^6 B16-HER2 (subcutaneously). Mice were treated with AdV5–IL-12 and/or AdV5-CCL5 on days 11, 13, and 15 (tumor size of 30 to 70 mm³). On day 16 after inoculation, tumors were isolated and single-cell suspensions were analyzed by flow cytometry or embedded in OCT and analyzed by multiparameter IF microscopy. $N = 1$. Number of cDC1s (CD11c⁺, F4/80⁻, Ly-6G⁻, MHCII⁺, CD103⁺, and CD11b^low) and (**H**) PD-L1 and CD80 expressing cDC1s. (**I**) Interaction count per square millimeter of CD8 T cells in close proximity to DCs. Representative IF pictures are showing AdV5–IL-12 + AdV5-CCL5–treated tumors (MHCII, red; CD11c, green; CD8, blue). White arrows are showing CD8 T cells (CD45⁺ and CD8⁺) neighboring DCs (CD45⁺, CD11c⁺, and F4/80⁻). (**J**) Ratio of PD-1, CD25, and CD69 expression on the CD8 T cell cluster in close (<50 μm) or distant (>50 μm) proximity to DC cluster. (**K**) Proportion of GzmB⁺ of CD8 T cells (CD3⁺, CD4⁻, and NKp46⁻ CD19⁻). (**L**) Batf3 knockout (KO) mice (lacking cDC1s) were engrafted with 0.5×10^6 B16-HER2 (subcutaneously). Mice were treated with AdV5–IL-12 and/or AdV5-CCL5. Tumor growth curves are shown. $n = 11$ mice per condition. Pooled data from two independent experiments. *$P < 0.05$, **$P < 0.01$, ***$P < 0.001$, and ****$P < 0.0001$. Error bar values represent SEM. For survival analysis, P values were computed using the log rank test. Two-way ANOVA was used to compare tumor growth curves.
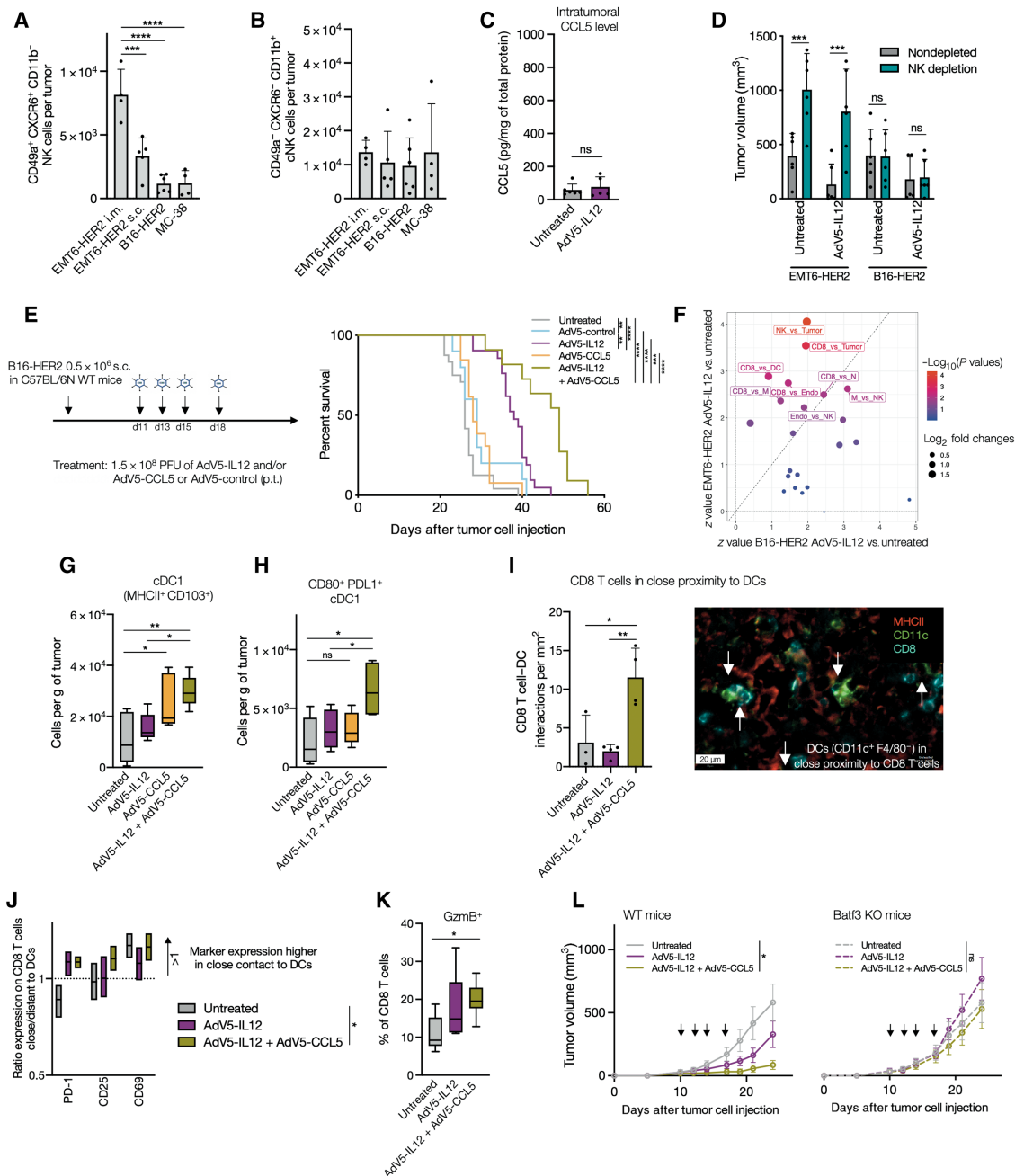
by IL-12. Next, we asked whether CCL5 supplementation in CD49a^{+} CXCR6^{+} NK cell[poor] B16-HER2 tumors could induce DC-CD8 T cell cross-talk and, therefore, promote antitumor T cell immunity. Using multicolor flow cytometry, we were able to detect increased numbers of cDC1s when tumors were treated with either AdV5-CCL5 alone or in combination with AdV5–IL-12 (Fig. 3G). Accordingly, we found an increased number of cDC1s expressing CD80 and PD-L1 in the AdV5-CCL5–AdV5–IL-12 combination (Fig. 3H and fig. S6, B and C), which indeed led to more interactions between DCs and CD8 T cells (Fig. 3I). In agreement, we observed more activated CD8 T cells in proximity to DCs (Fig. 3J) and an increased proportion of GzmB[+] CD8 T cells (Fig. 3K). In addition, we could observe an increased number of interactions between DCs and tumor cells (fig. S6C). To further understand the contribution of DCs to the therapeutic efficacy of the AdV5–IL-12 + AdV5-CCL5 combination, we used Batf3 knockout (KO) mice lacking cDC1s (30). The beneficial effect of AdV5–IL-12 ± AdV5-CCL5 on tumor control and survival was lost in Batf3 KO mice (Fig. 3L). Together, these data suggest that cDC1s attracted by CCL5 are essential for IL-12–mediated therapeutic benefit by enhancing T cell–mediated immunity; CCL5 can be provided by endogenous NK cells or be therapeutically supplemented in a CD49a^{+} CXCR6^{+} NK cell[poor] environment.

To show the potential of our adenoviral vector as a platform for combinatorial approaches, we then designed adenoviral vectors expressing both IL-12 and CCL5 (fig. S6D). To avoid deletion of IL-12 or CCL5 by homologous recombination, we encoded both transgenes under the control of orthogonal promotors, cytomegalovirus (CMV) or simian virus 40 (SV40) promoter. We were able to demonstrate similar therapeutic efficacy by expressing both payloads within one viral vector, independent of the choice of the promotor, although we thereby decreased the total viral load per injection (fig. S6, E and F).

AdV5–human IL-12 induces CCL5 expression in CD49a^{+} CD16^{−} NK cells in patient-derived tumor cultures

To test whether a human IL-12–encoding HER2-targeted and HER2-shielded adenoviral vector (AdV5-huIL12) can induce similar antitumor effects in a human ex vivo system, we cocultured primary tumor suspensions from patients with non–small cell lung cancer (NSCLC) (Fig. 4A) with a HER2-expressing ovarian cancer cell line (OVCAR3), which was transduced with AdV5-huIL12 (Fig. 4, A to E). This experimental system has been shown to activate primary human lymphocyte subsets and trigger human cancer cell killing in response to PD-1/PD-L1 blockade (31). Within patient-derived TILs and OVCAR3 cocultures, AdV5-huIL12 reduced OVCAR3 viability because of enhanced tumor cell killing (Fig. 4B). This effect was accompanied by an increase in IFN-γ secretion (Fig. 4C) and induction of IFN-γ–expressing patient-derived CD8 T cells and NK cells (Fig. 4D). In line with our murine data, CCL5 was up-regulated in NK cells by IL-12, which we confirmed by depletion of NK cells in the coculture system (Fig. 4E).

Next, we assessed the activity of AdV5-huIL12 using a human patient-derived tumor fragment model that preserves the tumor microenvironment and architecture but enables ex vivo perturbation by checkpoint blockade (32). Tumor fragments of HER2-expressing ovarian cancer samples embedded in Matrigel (Fig. 4F and fig. S7A) were transduced with AdV5-huIL12. In all four tested patients, we noticed increased staining for IFN-γ in CD8 T cells and CCL5 in

NK cells (fig. S7B); the latter was confirmed in the supernatant by enzyme-linked immunosorbent assay (ELISA) (Fig. 4G).

The identification of NK cells with tissue-resident traits as the main producers of CCL5 in the murine tumor models above prompted us to characterize which human tumor-infiltrating NK cells are producing CCL5. We therefore investigated the heterogeneity of tumor-infiltrating NK cells in patients with NSCLC using a published single-cell RNA sequencing (scRNAseq) dataset (33). We identified two main NK cell subsets with distinct gene expression profiles with the NK2 subcluster showing a higher expression of CCL5 compared to the NK1 subcluster (Fig. 4, H and I, and fig. S8, A and B). Recently, NK core signature genes associated with cytokine-producing phenotype (CD56^{bright} CD16^{−}) or tissue residency have been described (34, 35). We noticed an enrichment of CD56^{bright} CD16^{−} and tissue residency genes in the CCL5-enriched NK2 subcluster (Fig. 4J). Core tissue residency signature genes included up-regulation of the integrin ITGA1 (CD49a), ITGAE (CD103), CD69, and ENTPD1 (CD39), which distinguish NK2 from the highly FCGR3A (CD16)–expressing NK1 subtype (fig. S8, C to F). To investigate whether IL-12 induces CCL5 production in NK cells with tissue residency characteristics (CD49a^{+} CD16^{−}), we characterized human tumor-infiltrating NK cells producing CCL5 in our coculturing system (Fig. 4A and fig. S8). In line with our findings from mouse tumor models, CD49a^{+} CD16^{−} NK cells were producing higher amounts of CCL5 in response to AdV5-huIL12 compared to CD16^{+} CD56^{dim} cNK cells (Fig. 4M). Collectively, these experiments recapitulate our finding that IL-12 can directly stimulate the antitumor activity of tumor-infiltrating T cells and induce CCL5 up-regulation in NK cells with tissue-resident traits in primary human tumors.

CCL5 expression by NK cells with tissue-resident traits enhances the efficacy of PD-1 blockade

It has been demonstrated that IL-12–producing DCs, activated by IFN-γ–secreting CD8 T cells, are critical for successful responses to anti–PD-1 treatments (5). This led us to investigate whether the DC attractant CCL5 is associated with efficient tumor responses to anti–PD-1 therapy.

In patients with melanoma undergoing nivolumab treatment (36), we compared CCL5 induction during treatment between patients who were responding (R) and nonresponding (NR) (Fig. 5A). CCL5 up-regulation was associated with clinical responses (Fig. 5B). Furthermore, we noticed a positive correlation between the NK2 signature and CCL5 expression (Fig. 5C) (9). We also found a positive correlation between the level of CCL5 and cDC1s in patients with treated melanoma (Fig. 5D). These findings suggest that CCL5 may be produced by intratumoral NK cells in response to PD-1 blockade and, subsequently, might promote cDC1 recruitment, which is in accordance with our observation in tumor models after IL-12 treatment.

To further investigate this possibility, we used the patient-derived tumor fragment platform, which allowed us to dissect the early immunological response of human tumor tissue to PD-1 blockade (37). We measured IFN-γ and CCL5 in the supernatants of tumor fragments from patients with cancer exposed to anti–PD-1 (Fig. 5E). In line with the correlative analysis of clinical trial data (Fig. 5B), we found increased CCL5 secretion in responding tumor fragments (defined by increased IFN-γ secretion) with anti–PD-1 blockade (Fig. 5, F and G).
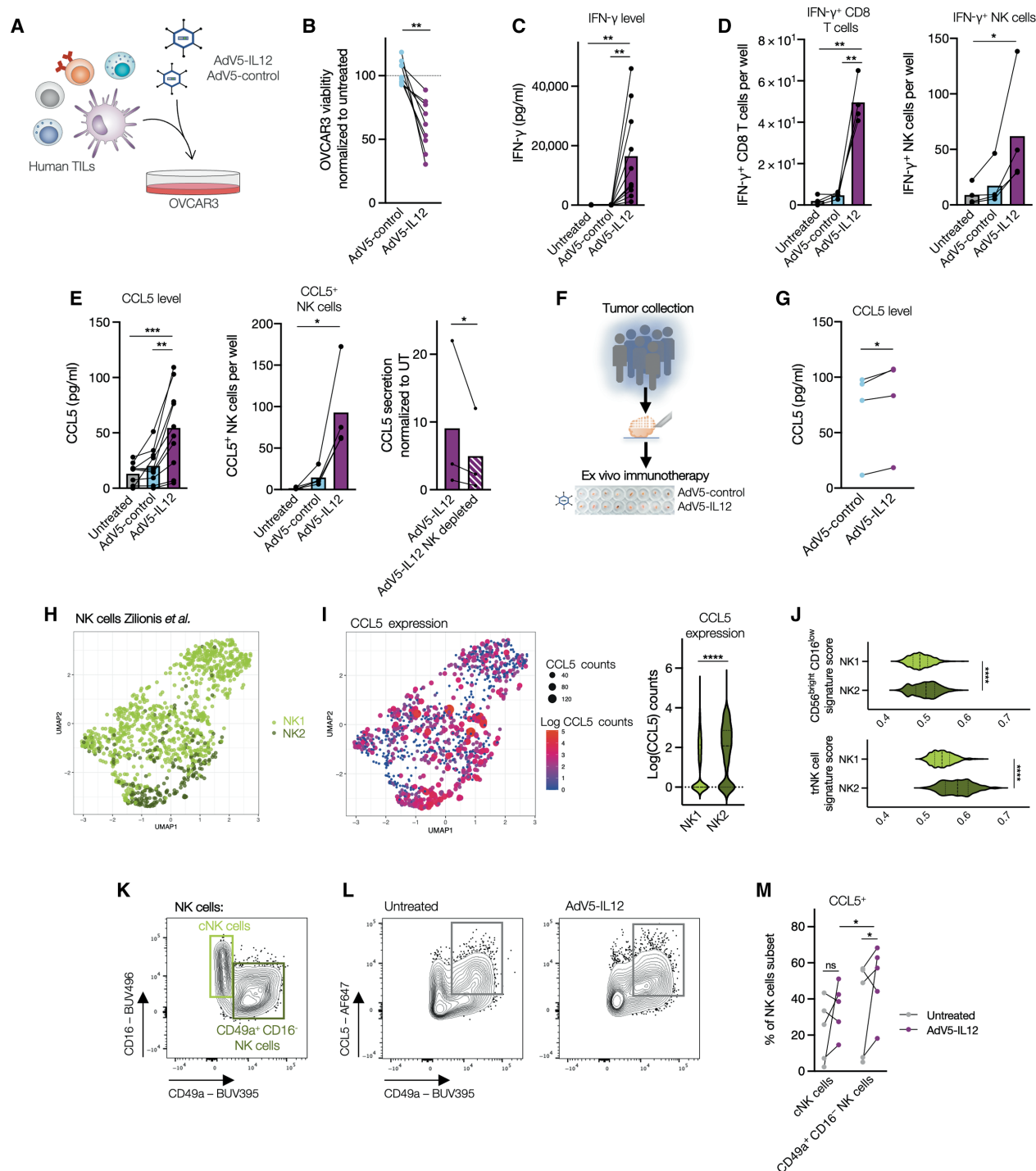
Fig. 4. AdV5-huIL12 induces CCL5 expression in CD49a$^+$ CD16$^-$ NK cells in patient-derived tumor cultures. (**A**) Tumor digests of patients with NSCLC were cocultured with OVCAR3 cells, which were transduced with HER2-targeted AdV5 encoding human IL-12 or control virus. $N = 2$. (**B**) Quantification of OVCAR3 viability normalized to untreated cocultures after 96 hours. (**C**) IFN-γ expression was determined in supernatants after 5 days. (**D**) Cell count of IFN-γ$^+$ CD8 T cells (CD3$^+$ and CD56$^-$) and NK cells (CD56$^+$ and CD3$^-$) per well after 96 hours. (**E**) Cell count of CCL5$^+$ NK cells (CD56$^+$ and CD3$^-$) after 96 hours and CCL5 expression in supernatants after 5 days. UT, untreated. (**F**) HER2$^+$ ovarian cancer samples were dissected into tumor fragments and cultivated and embedded in Matrigel. Tumor fragments were treated with HER2-targeted AdV5 encoding human IL-12 for 48 hours (8 to 12 fragments per condition). (**G**) CCL5 concentration in supernatant was analyzed by ELISA. (**H**) UMAP projection of scRNAseq data of tumor-infiltrating NK cells of patients with NSCLC is shown. (**I**) *CCL5* expression in NK1 and NK2 subpopulations was quantified. (**J**) CD56^{bright}CD16^{low} and tissue-resident NK (trNK) cell signature scores of NK1 and NK2 were determined. (**K** to **M**) Tumor digests of patients with NSCLC were cocultured with OVCAR3 cells, which were transduced with HER2-targeted AdV5 encoding human IL-12. (K) NK cell subsets were defined by CD16 and CD49a expression. (L) CCL5-producing NK subsets were visualized after AdV5–IL-12 treatment (right) compared to untreated (left). (M) Percentage of CCL5$^+$ NK cell subsets was quantified. *$P < 0.05$, **$P < 0.01$, and ***$P < 0.001$. Error bar values represent SD. Paired two-tailed Student's t test was used. For comparisons between three or more groups, one-way ANOVA with multiple comparisons was used.
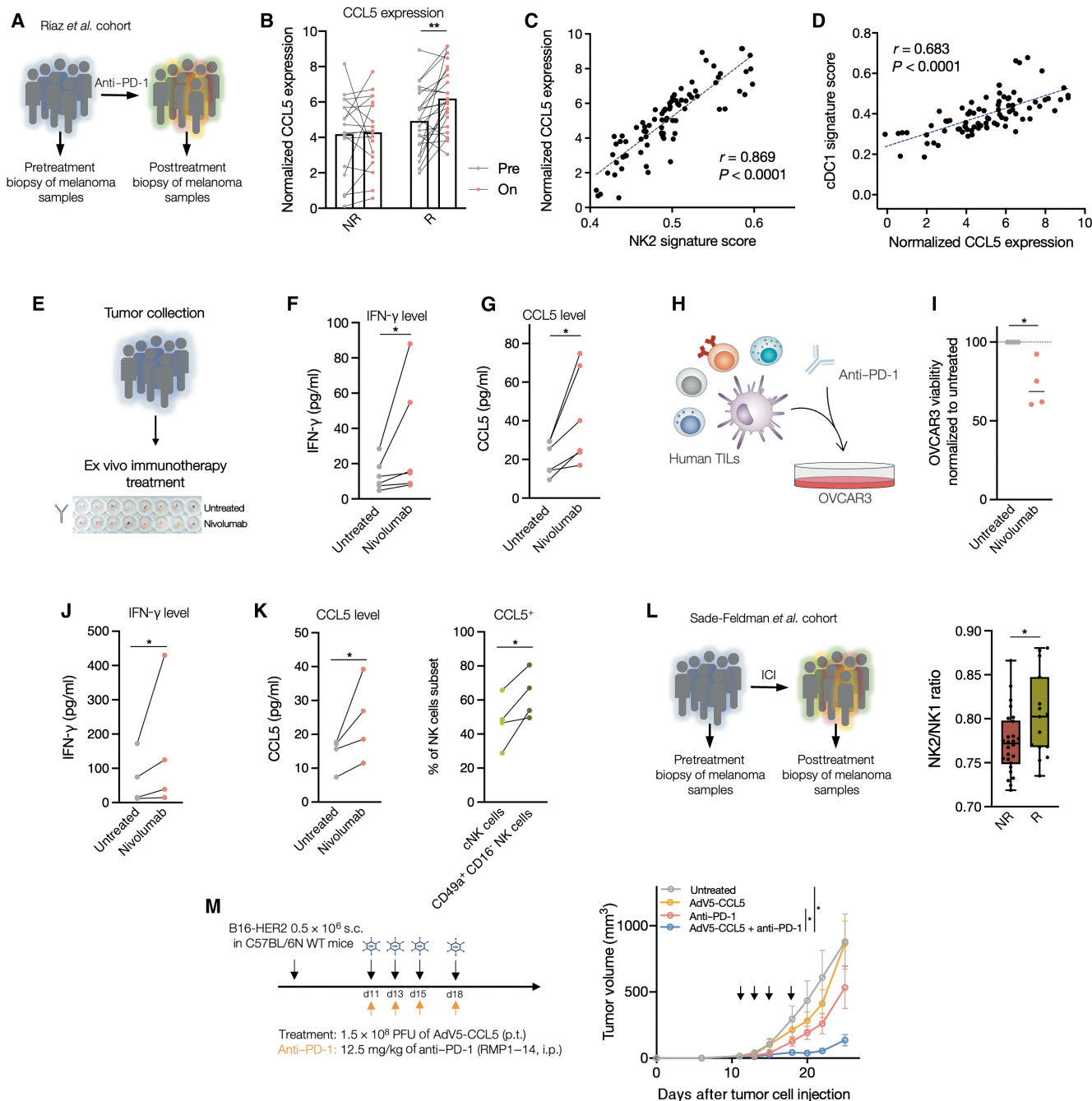
Fig. 5. CCL5 expression by NK cells with tissue-resident traits enhances the efficacy of PD-1 blockade. (**A**) CCL5 expression in tumor biopsies of patients with melanoma (n = 42) was analyzed before and during nivolumab treatment (36). (**B**) Normalized expression of *CCL5* before (pre) and during (on) nivolumab treatment between patients with no response (NR) or response (R = SD + PR + CR) was quantified. (**C**) Correlation between *CCL5* expression and NK2 signature score or (**D**) cDC1 signature score is shown. (**E**) Cancer samples were dissected into tumor fragments and cultivated and embedded in Matrigel. Tumor fragments were treated with nivolumab for 48 hours (six to eight fragments per condition). (**F**) IFN-γ and (**G**) CCL5 were determined in the supernatant. n = 6 tumor samples. (**H**) Tumor digests of patients with NSCLC treated with nivolumab were cocultured with OVCAR3 cells for 48 hours. (**I**) OVCAR3 viability was normalized to the untreated control group. (**J**) IFN-γ and (**K**) CCL5 were determined in the supernatant. Percentage of CCL5+ NK cells was quantified after nivolumab treatment. (**L**) NK2/NK1 ratio of patients with no response (NR: PD) versus response (R: SD + PR) before and after treatment with ICI. (**M**) WT mice were engrafted with 0.5×10^6 B16-HER2 (subcutaneously). Mice were treated with AdV5-CCL5 (peritumorally) as indicated by black arrows and/or anti–PD-1 (intraperitoneally) antibodies on days 11, 13, 15, and 18 (tumor size of 30 to 70 mm^3) as indicated by orange arrows. Tumor growth curves are shown. n = 6 mice per condition. N = 1. *P < 0.05, **P < 0.01. Error bar values represent SD or SEM (tumor growth curves). Paired two-tailed Student's t test was used. For comparisons between three or more groups, one-way ANOVA with multiple comparisons was used. Two-way ANOVA was used to compare tumor growth curves.

We next cocultured human TILs with OVCAR3 cells in combination with anti–PD-1 (Fig. 5H). Anti–PD-1 treatment resulted in high concentrations of IFN-γ and CCL5 in the supernatants and resulted in enhanced killing of OVCAR3 cells (Fig. 5, I to K). The proportion of CCL5$^+$ cells was higher in the CD49a$^+$ CD16$^-$ NK cells compared to cNK cells in cocultures exposed to anti–PD-1 (Fig. 5K), which confirms NK cells with tissue-resident traits as the main source of immunotherapy-induced CCL5.

To further underline the beneficial response of CCL5-producing, tissue-resident NK2 cells upon PD-1 blockade, we reanalyzed a scRNAseq dataset of patients with melanoma treated with immune checkpoint inhibitors (ICIs) (37). We calculated the ratio of NK2 versus NK1 signature scores for each NK cell as a surrogate for NK2 characteristics while controlling for NK cell abundancy. We observed that the NK2 phenotype was enriched in patients showing clinical responses (Fig. 5L).

Last, we asked whether CCL5 can further boost anti–PD-1 therapy in CD49a$^+$ CXCR6$^+$NK cell^{poor} tumors. We combined anti–PD-1 therapy with the adenoviral vector encoding CCL5 in B16-HER2–bearing mice (Fig. 5M). Whereas AdV5-CCL5 single treatment did not show any therapeutic efficacy, we observed increased therapeutic effects when combined with anti–PD-1 treatment. Together, these data demonstrate that CCL5 production by NK cells is important for the response to PD-1 blockade, and CCL5-supplementing therapies can enhance the efficacy of PD-1 blockade in CD49a$^+$ CXCR6$^+$NK cell^{poor} tumors.

DISCUSSION

Multimodal immunotherapy combinations that target diverse immune-tumor interactions have become a cornerstone in the therapeutic management of patients with different cancer types and are being extensively explored to maximize the clinical benefit of cancer immunotherapies (38–41). Here, we identify the lack of NK cells with tissue-resident traits as an unrecognized barrier to treatment effectiveness of targeted IL-12 and anti–PD-1 therapy (fig. S9). We show that IL-12 enhanced antitumorigenic DC-CD8 T cell interactions, which relied on CD49a$^+$ CXCR6$^+$ NK cell–specific induction of CCL5. In tumor models with a limited number of those NK cells and thus low CCL5 expression, only moderate IL-12 responses were observed. However, responses of CD49a$^+$ CXCR6$^+$ NK cell^{poor} tumors could be rescued by concomitant administration of a CCL5-encoding adenoviral vector, which—after converting tumor cells into CCL5 production sites—induced cDC1 infiltration and thus increased DC-CD8 T cell interactions. Because of the unique role of cDC1s in the initiation of T cell responses, both de novo and upon anti–PD-1 checkpoint inhibition, we subsequently observed that CCL5 produced by NK cells drives the response to anti–PD-1 therapy, which can be delivered using the AdV5 platform. These findings could be used to improve immunotherapy by fine-tuning the cross-talk between lymphoid and myeloid immune compartments using multimodal combination immunotherapies adjusted to the preexisting tumor microenvironment of each patient.

Viral vectors have been shown to be a suitable tool for local immunotherapy, reducing the systemic spread of therapeutic agents and consequently avoiding systemic side effects (42). Our adenoviral platform uses exogenously added retargeting adapters consisting of designed ankyrin repeat proteins (DARPins) (43). This strategy has unique advantages, compared to targeting by genetic modifications, including the large existing library of DARPins and the rapid selection of new DARPin adapters against any given surface protein (44, 45).

Here, we targeted the model tumor-antigen HER2, which is overexpressed in different cancer types (46). To further broaden the clinical applicability, DARPins may be selected to specifically recognize targets on cells other than tumor cells, such as tumor-associated antigens on stromal cells (47, 48). Recently, the development of high-capacity, helper-dependent AdVs has enabled the expression of transgenes of up to 36 kilobase pairs. This, in combination with the targeted and shielded strategy, has increased the potential of AdVs as an ideal vector for multimodal cancer immunotherapy (21, 22). Previous work has shown that adenoviral vectors can act as a "self-adjuvants," allowing the stimulation of multiple innate immune signaling pathways such as Toll-like receptors and the induction of type I IFNs upon viral entry (49–51). Whereas these effects may explain the effect of the empty AdV5-control in tumor delay, the improved antitumor immunity supports the potential advantage of adenoviral vectors compared to other gene delivery vectors (52, 53).

A variety of factors and cell types in the tumor microenvironment underpin the clinical success of cancer immunotherapies, and untangling these complex interactions is critical to understand and improve therapeutic efficacy (54). Although typically rare, DCs play a key role in orchestrating antitumor immunity. Consequently, intratumoral presence of DCs and particularly production of IL-12 have been associated with better survival in various cancer types and are positively correlated with clinical outcome to anti–PD-1 therapy (2). Therefore, IL-12 has been extensively investigated for use in cancer immunotherapy. We here demonstrate that IL-12, provided intratumorally by paracrine AdV5 delivery, is capable to bridge innate and adaptive immunity. As a consequence of IL-12 produced by tumor cells after treatment, CD8 T cells increased their activation and cytotoxic potential, as demonstrated in tumors from patients and in tumor models. In the latter, early tumor growth control is achieved by the steady state of lymphocytes present within the tumor. However, to achieve long-term tumor rejection, lymphocyte and antigen trafficking to draining lymph nodes is needed. In agreement, we observed increased numbers of NK cells and CD8 T cells in close proximity to blood vessels, which suggests enhanced trafficking from the periphery to the tumor. This may be induced by the observed CCL5 secretion by CD49a$^+$ CXCR6$^+$ NK cells or other IFN-γ–induced chemokines such as CXCL9 and CXCL10. Moreover, the fact that cDC1s have been described as the main source of CXCL9 and CXCL10 (55) could subsequently explain the increased interactions between CD8 T cells and DCs, which have initially been attracted to the tumor microenvironment by CCL5. Consequently, we demonstrated that AdV5–IL-12 not only improves lymphocyte homing and activation in the primary tumor but also promotes abscopal antitumor effects at distant tumor sides.

NK cells contribute to various immune functions during cancer initiation and progression. Investigations of NK cells have originally emphasized their cytotoxic potential, particularly in the context of tumor immunity. Mature potent cytolytic effector CD56^{dim}CD16^{high} cNK cells, rapidly secreting proinflammatory cytokines and cytotoxic mediators upon receptor-mediated activation, have therefore been considered as the main subpopulations mediating tumor immunity. Tissue-resident NKs, in contrast, show reduced cytotoxic potential, although being specialized on cytokine production such as tumor necrosis factor–α, granulocyte-macrophage colony-stimulating factor, and IL-2 secretion. They have been described to express increased amounts of inhibitory checkpoint receptors and were therefore rather associated with tissue homeostasis (56). In the context of cancer, they are poorly characterized and controversially discussed.

They have been associated with poor survival in human hepatocellular carcinoma, whereas, on the other hand, they are also reported to join forces with cNK cells to control liver metastasis (*57, 58*).

Here, we demonstrate that NK cells with tissue-resident traits and their expression of CCL5 were essential for the efficacy of AdV5–IL-12 and furthermore correlated with response to anti–PD-1 in patients with melanoma. Although we observed expression of CCL5 in cNK cells and CD49a$^+$ NK cells in the steady state, CD49a$^+$ NK cells specifically up-regulated CCL5 in response to AdV5–IL-12 and anti–PD-1 treatment in mice and human tumor specimens. Therefore, we uncovered a role of NK cells with tissue-resident traits in priming the tumor immune microenvironment by inducing DC-CD8 T cell interactions and provide direct evidence that the lack of intratumoral cDC1 recruitment by NK cell population represents a major barrier for T cell–based therapies.

Some controversy exists regarding the role of CCL5 in cancer. A number of studies suggest that CCL5 has potential tumor-promoting effects, either by directly affecting tumor growth (*59*), fostering an immunosuppressive tumor microenvironment (*60*), enhancing tumor cell migration (*61*), or expanding cancer stem cells (*62*). In contrast, other studies show delayed tumor growth and prolonged survival in mouse models with CCL5-expressing tumor cells, as well as a correlation between CCL5 expression and a T cell–inflamed phenotype in patients with cancer (*63–65*). In our models, AdV5-CCL5 did not exhibit any tumor-promoting effects and also failed to show therapeutic benefits as a monotherapy. In agreement with previous work (*9*), AdV5-CCL5 treatment induced cDC1 recruitment. However, only the combination with AdV5–IL-12 led to higher costimulatory potential and subsequently increased tumor-reactive T cells. This suggests that the antitumorigenic properties of CCL5 are likely context dependent: In the presence of other antitumorigenic signals induced by IL-12 or anti–PD-1 treatment, which are known to tip the balance to a proinflammatory environment, CCL5 may further boost these effects, which then translates into improved responses as evidenced by our in vivo data and analysis of patient cohorts. Besides CCL5, XCL1 has been described to have similar capacities in recruiting cDC1s to the tumor bed while not being reported to have tumor-promoting capacities (*9*). On this note, XCL1 might be an intuitive alternative payload to guide cDC1s into tumors to improve antitumor immunity.

Our study contains some limitations. Whereas our study provides a phenotypical description of a population of CCL5-expressing NK cells with tissue-resident traits, it does not resolve its origin, transcriptional regulation, and particularly its tissue retention. Furthermore, this here described that NK cell population shares phenotypic features with both tissue-resident NK cells and type 1 lymphoid cells (*66*). Single-cell transcriptomics of tumor-infiltrating innate cells has recently advanced our understanding by revealing broad transcriptional clusters with a fluent transition between both cell types instructed by the tumor microenvironment (*25, 57*). It will be of considerable interest in future studies to investigate the transcriptional regulation and effector differentiation of innate lymphocytes in tumors including the here described CCL5-producing cells. This will be instrumental in defining their lineage relationship and further resolves whether distinct functions can be assigned to a certain subtype. Particularly in patients treated with immunotherapy, niche-dependent or tumor-derived factors need to be identified that mediate resistance by limiting the accumulation, differentiation, survival, and function of these cells within the tumor microenvironment.

Such factors may serve as predictive markers for T cell–focused therapies and define the need for potential combinations with cDC1-attracting agents such as CCL5, which allows to improve the efficacy of IFN-γ–inducing therapies including IL-12 and checkpoint inhibition in tumors.

Together, our data highlight the importance of NK cells with tissue-resident traits and their capability to induce T cell immunity by enhancing DC–T cell cross-talk in IFN-γ–inducing therapies and may inform combination strategies using viral vector platforms as an approach to further potentiate this NK cell–DC–T cell cross-talk. Our data highlight a relevant tumor-eliminating positive feedback mechanism to be prioritized for clinical development, particularly in patients with immune-excluded or immune-resistant tumors.

MATERIALS AND METHODS
Study design
These experiments were designed to evaluate the efficacy and resistance mechanisms of local IL-12 therapy in solid tumors in mice. Specifically, experiments were focused to identify soluble factors and their producer cells in the tumor microenvironment, which restrict IL-12 response to finally overcome resistance by additional production of those factors using the here described adenoviral platform. The immunocompetent murine studies were complemented by in vitro experiments using primary human tumor material to confirm findings in a human setting. We used flow cytometry, multiparameter microscopy, ELISAs, and in vivo depletion/neutralization studies to identify resistance mechanisms. The investigators were not blinded to the allocation of groups during experiments or subsequently during the analysis. Although statistical methods were not used to predetermine sample size, sample sizes were chosen on the basis of estimates from pilot experiments and previously published results. Animals were randomized to treatment groups after tumor implantation based on tumor size (30 to 70 mm^3) at the treatment start point. For cellular assessments, lymph node–contaminated tumor digests were excluded, defined by a B cell proportion of more than 20% of all CD45$^+$ alive cells. The *n* values and particular statistical methods are indicated in the figure legends and at the "Statistical analysis" section.

Redesign of AdV5 shuttle vector
The pShuttle vector from the AdEasy Adenoviral Vector System (Agilent Technologies) was redesigned to allow for the rapid generation and exchange of modular expression cassettes, encoding a variety of payloads (*67*). The multiple cloning site (MCS) of the pShuttle vector was replaced with synthetic MCS modules, called MCS1 or MCS2, by Gibson Assembly (New England Biolabs). The synthetic MCS1 module contained, from 5′ to 3′, the CMV promoter, Nhe I restriction site, Xho I restriction site, and polyadenylate [poly(A)] site from bovine growth hormone as previously described (*20*). The MCS2 module contained, from 5′ to 3′, the SV40 promoter, Spe I restriction site, Sal I restriction site, and poly(A) site from SV40. MCS modules were synthesized by GeneArt (Life Technologies Europe BV) containing the N-terminal flanking DNA 5′-GAA TAA GAG GAA GTG AAA TCT GAA TAA TTT TGT GTT ACT CAT AGC GCG TAA-3′ and C-terminal flanking DNA 5′-TAA GGG TGG GAA AGA ATA TAT AAG TGG GGG GTC-3′ for Gibson Assembly into pShuttle to generate the plasmids pShuttle-MCS1 or pShuttle-MCS2. In addition, a plasmid called pShuttle-MCS1-MCS2

was constructed, where both the MCS1 and MCS2 modules were inserted in tandem into the same pShuttle construct.

Construction of payload construct

Murine and human IL-12 constructs were generated from translated GenBank complementary DNA sequences for the IL-12B/p40 [National Center for Biotechnology Information (NCBI) reference: BC103608.1 or BC074723.2, respectively) and IL-12A/p35 (NCBI reference: BC146595.1 or BC104984.1, respectively) connected by a F2A peptide as previously described (21). The murine CCL5 gene was generated from the UniProt sequence P30882. Cytokines included their native signal sequences, were codon-optimized for human or mouse expression, and were synthesized by GeneArt (Thermo Fisher Scientific). For reporter assays, a firefly luciferase reporter was synthesized from GenBank: BAL46512.1. Payload constructs were inserted into the redesigned pShuttle vectors by Gibson Assembly or standard ligation cloning to generate pShuttle-MCS1 including the payload. The pShuttle-MCS1 backbone (without payload) was used to generate the AdV5-control vector. In general, pShuttle-MCS1-IL12 (AdV5–IL-12), pShuttle-MCS1-CCL5 (AdV5-CCL5), and pShuttle-MCS1-Luciferase (AdV5-Luc) were used to generate immunotherapeutic vectors. For the combinatorial approach optimization (fig. S7, D to F), pShuttle-MCS2-CCL5 (AdV5-SV40-CCL5) and pShuttle-MCS2-IL12 (AdV5-SV40-IL12) as well as pShuttle-MCS1-IL12-MCS2-CCL5 (AdV5-CMV-IL12-SV40-CCL5) and pShuttle-MCS1-CCL5-MCS2-IL12 (AdV5-CMV-CCL5-SV40-IL12) were used.

Virus production

The plasmid containing the adenoviral genome, pAdEasy-1, from the AdEasy Adenoviral Vector System (Agilent Technologies) was previously modified to include a mutation to the hypervariable loop 7 (HVR7) of the hexon, which prevents blood factor X binding to virions and thus reduces liver infection (22). To generate viral constructs, the modified pAdEasy-1_HVR7 plasmid was cotransformed with the pShuttle-MCS variants listed above into recA-proficient *Escherichia coli* BJ5183 cells, from which the desired recombinants, obtained by homologous recombination, could be isolated for virus production. Packaging and amplification of adenoviral particles were performed by Vector Biolabs, and they were purified on two consecutive cesium chloride density gradients and provided directly in phosphate-buffered saline (PBS) with 5% glycerol.

Protein purification of adenoviral shield and retargeting adapter

The human HER2 adenoviral retargeting adapter (G3_1D3nc_SHP1) was expressed and purified as previously described (22, 44). Endotoxin was removed from purified adapters using the Endotrap HD Endotoxin Removal System (Hyglos GmbH), and adapters were stored at −80°C in endotoxin-free Dulbecco's PBS (Millipore, TMS-012-A). The adenoviral shield was purified in Sf9 insect cells as previously described (22).

Mice

C57BL/6 and Balb/c mice were bred in-house at University Hospital Basel, Switzerland. Batf3 KO [B6.129S(C)-Batf3<tm1Kmm>/J] mice were obtained from the Jackson Laboratory, USA. Animals were housed under specific pathogen–free conditions. All animal experiments were performed in accordance with Swiss federal regulations.

Sex-matched littermates at 8 to 12 weeks of age at the start of experiments were used.

Tumor models

A total of 0.5×10^6 syngeneic murine B16 D5 melanoma cells expressing HER2 (provided by L. Weiner, Georgetown University, Washington, DC) or MC-38 colon carcinoma cells suspended in phenol red–free Dulbecco's modified Eagle's medium (without additives) were injected subcutaneously into the right flank of C57BL/6 and Batf3 KO mice. EMT6 murine breast cancer cells expressing HER2 (1×10^6) were injected subcutaneously or into the mammary gland of female Balb/c mice (68). Cell lines were tested for mycoplasma contamination before injection. Tumor volume was calculated according to the following formula: $D/2 \times d \times d$, with D and d being the longest and shortest tumor diameter in millimeters, respectively.

Immunotherapy treatments

Tumor-bearing mice, with a tumor size of about 30 to 70 mm^3, were each treated with 1.5×10^8 PFU of HER2-targeted and HER2-shielded adenoviral vectors in 50 μl of PBS (peritumorally) and/or mouse anti–PD-1 (RPM1–14, Bio X Cell) or left untreated. For depletion studies, CD8 T cells were depleted by administering anti-CD8a (53-6.72, Bio X Cell) at 10 mg/kg (intraperitoneally) once per week. NK depletion was performed by administering anti-AsialoGM1 (Poly21460, BioLegend) 50 μl (intraperitoneally) in Balb/c mice or anti-NK1.1 (PK136, Bio X Cell) 10 mg/kg (intraperitoneally) in C57BL/6 mice every 4 to 5 days. IFN-γ neutralization was performed using an anti–IFN-γ antibody (XMG1.2, Bio X Cell) at 25 mg/kg in 200 μl of PBS injected every 2 to 3 days. To neutralize CCL5, we injected 32 μg of anti-CCL5 antibody (500-P118, Pepro-Tech) in 200 μl of PBS per mouse intraperitoneally. Depletion and neutralization schedules were started the day before immunotherapy treatment unless stated otherwise.

Bilateral tumor models

Balb/c mice were inoculated with 1×10^6 EMT6-HER2 tumor cells (intramammary) in the right flank. Four days later, 0.25×10^6 EMT6 WT cells were injected into the contralateral site (intramammary). On days 7, 9, 11, and 13 after the first tumor inoculation, EMT6-HER2 tumors were each treated with 1.5×10^8 PFU of HER2-targeted and HER-shielded adenoviral vector encoding IL-12 in 50 μl of PBS (peritumorally). Tumor volumes of contralateral (EMT6 WT) tumors were measured.

Tumor rechallenge

Long-term surviving mice from AdV5–IL-12 therapy were rechallenged with EMT6 WT and EMT6-HER2 tumors in each flank for 60 days after primary tumor rejection. EMT6 WT and EMT6-HER2 rechallenge doses were 0.25×10^6 cells and 1×10^6 cells, respectively. As a control, naive Balb/c mice were implanted alongside rechallenged mice.

FTY720 treatments

Mice were implanted with EMT6-HER2 or B16-HER2 tumors intramammary or subcutaneously, respectively. Mice were treated or not with FTY720 (1.25 mg/kg) (Cayman Chemical) intraperitoneally daily throughout the duration of the experiment. Injections were started 1 day before tumor inoculation or the day before adenoviral treatment.

In vivo pharmacokinetic experiments

Mice were implanted with EMT6-HER2 or B16-HER2 tumors intramammarily or subcutaneously, respectively. Once the tumors reached an average volume of 30 to 70 mm^3, luciferase-encoding retargeted and shielded AdV5 (1.5×10^8 PFU per mouse; AdV5-Luc) were injected peritumorally. The luciferase signal was determined in live animals 1 day after virus injection and 10 min after intraperitoneal injection of D-luciferin (150 mg/kg) (PerkinElmer) using the in vivo imaging system NightOWL II LB 983 (Berthold) over 2 weeks. After live imaging, luciferase activity was determined in isolated tumors and organs (draining and nondraining lymph nodes, spleen, liver, kidney, lung, and heart). The overlay of the real image and the luminescence representation allowed the localization and measurement of luminescence emitted from xenografts. The signal intensities from manually derived regions of interest (ROIs) were obtained, and data were expressed as photon flux (photons per second). All measurements were performed under the same conditions, including camera settings, exposure time (60 s), distance from lenses to the animals, and ROI size.

Multiparameter flow cytometry

Tumor tissue was isolated from mice, weighed, and minced using razor blades. Tissue was then digested using Accutase (PAA Laboratories), collagenase IV (Worthington), hyaluronidase (Sigma-Aldrich), and deoxyribonuclease (DNAse) type IV (Sigma-Aldrich) for 60 min at 37°C with constant shaking. The cell suspensions were filtered using a cell strainer (70 μm). Precision Count Beads (BioLegend) were added before staining to quantify the number of cells per gram of tumor. Single-cell suspensions were blocked with rat anti-mouse FcγIII/II receptor (CD16/CD32) blocking antibodies ("Fc-Block") and stained with live/dead cell exclusion dye (Zombie UV dye, BioLegend). The cells were then incubated with fluorophore-conjugated antibodies (table S1) directed against cell surface antigens, washed, and resuspended in fluorescence-activated cell sorting buffer [PBS + 2% fetal bovine serum (FBS)]. For intracellular/intranuclear antigens, cells stained with cell surface antibodies were fixed and permeabilized using Foxp3/transcription factor staining buffer set (eBioscience) before incubation with antibodies directed against intracellular antigens. Cell populations were analyzed on Cytek Aurora and CytoFLEX.

Bioinformatic analysis of flow cytometry data

Forward scatter (FSC) files containing pregated alive CD45$^+$ single cells were read into R using the flowCore package (flowCore: flowCore: Basic structures for flow cytometry data version 2.2.0 from Bioconductor) (69). A logicle transform was performed per channel, with parameters calculated from aggregated data from all samples. CD45-low cells with a transformed value of <2.5 were removed from further analysis (threshold set on the left side of the trough of the density plot of transformed CD45 values from all samples). The measurements were randomly subsampled to 1.5×10^5 cells per condition to expedite downstream operations. Principal components analysis (PCA) was performed using all markers except for CD45, Live-Dead, forward scatter (FSC) and sideward scatter (SSC). Uniform manifold approximation and projection (UMAP) was performed for visualization using the CATALYST module's runDR function (CATALYST: Cytometry dATa anALYSis Tools version 1.14.0 from Bioconductor) (70). Clustering was performed using Rphenograph (0.99.1), an R implementation of PhenoGraph (GitHub, JinmiaoChenLab/Rphenograph:

Rphenograph: R implementation of the PhenoGraph algorithm) (71, 72). Five clusters with universally high expression across all markers were removed, and steps starting with PCA were repeated. Three resulting clusters were removed again, and the process iterated once more to yield the final clustering, UMAP, and heatmaps (73). The supplemental UMAP visualization of the scaled marker expression was done with CATALYST's plotDR function. Main cell types were assigned by marker expression. To confirm certain assignments, cell populations were gated using FlowJo (10.6.2) and compared to assigned populations, such as the following NK cells: NKp46$^+$, CD3$^-$, CD19$^-$ Ly-6G$^-$, and F4/80$^-$.

Multiparameter fluorescence microscopy

Tumors embedded in optimal cutting temperature compound (OCT) were sectioned into 7-μm-thick slices and attached to poly-L-lysine–coated square coverslips. Sections were analyzed using CODEX (Akoya Biosciences), a highly multiplexed imaging platform, which allows the staining of solid tissue sections with a panel of up to 40 antibodies at once (23). Briefly, CODEX uses a unique DNA barcode system to label each antibody clone individually. These barcodes can be detected by reversible hybridization to their corresponding reporter. The respective reporters, which are conjugated with the fluorophores Alexa Fluor 488 (AF488),, Atto550, or Cyanine-5 (Cy5), are applied onto the tissue sections, imaged, and removed in a multicycle experiment. For this purpose, the manufacturer's protocol "CODEX User Manual Rev A.0" (provided by Akoya Biosciences) was followed.

The antibody panel was composed of commercially available Akoya-conjugated antibodies and self-conjugated custom antibodies (CODEX Conjugation Kit, Akoya Biosciences; table S2). Tissue staining was performed with the CODEX Staining Kit (Akoya Biosciences). Briefly, the tissue was thawed with Drierite beads, fixed with acetone, rehydrated, and fixed with 1.6% paraformaldehyde (PFA). After blocking, the tissue was stained with the established antibody panel consisting of 33 barcoded antibodies at the same time. The bound antibodies were fixed to the tissue with 1.6% PFA, ice-cold methanol, and a fixative solution (Akoya Biosciences).

The inverse microscope DMi8 (Leica) was used for acquisition (×20 magnification, *xyz* acquisition mode 14 *Z*-stacks each 14.99 μm, "Best Focus" autofocus with default settings). The generated fluorescence data were formatted with the Akoya CodexDriver V2 and subsequently processed using the CODEX Processor (version v1.5.0.48b) or the Kheops plugin in ImageJ and QuPath 0.2.3 and StarDist (74–76). The processing steps included (i) *XY* processing with tile registration and shading correction; (ii) *Z*-stack processing with deconvolution, drift compensation, overlap cropping, background subtraction (min-min mode), and best focus detection; (iii) stitching with best focus interpolation and tile overlap of 10%; and (iv) cell segmentation on the nuclear stain with the radius 8 or threshold (0.69), channels ("DAPI"), normalize percentiles (1.99), pixel size (0.423), cell expansion (2.8), and cell constrain scale (1.5) in StarDist.

The processed and segmented data were analyzed with the CODEX Multiple Analysis Viewer (version 1.2.0.297) or the PhenoGraph algorithm using R 4.0.2. Manual gating was performed to distinguish between CD45$^+$ cells (immune cells) and CD45$^-$ cells (tumor and stroma cells). Clustering was performed with VorteX using unbiased hierarchical *X*-shift clustering ($K = 55$ resulting in 81 immune clusters) (77). Clusters were manually verified and assigned to main immune cell populations using the CODEX Multiple Analysis Viewer or QuPath. Subsequently, mean marker expression

and interaction counts between cellular main populations (cells with <50-μm proximity) were determined.

Interaction analysis

Interaction counts between main cell populations (contact defined as <50-μm proximity) were used for further analysis. The cluster "L" containing lymph vessels was excluded from further analysis because of the very distinct localization of its cells as small vessels. Expected interaction counts for each cell-cell interaction pair were calculated as

$$\text{expectedInteraction}_{CellA\_CellB} = \text{interaction}_{allCells} \times \text{frequency}_{CellA} \times \text{frequency}_{CellB}$$

Next, a negative-binomial generalized linear model for the interaction counts with an offset of log(expectedInteractions) was generated in R 4.0.2. The mathematical interaction terms between cell-cell type comparison (DC_vs_CD8) and experimental condition (untreated, AdV5-empty, and AdV5–IL-12) were used to calculate odds ratios and P values for changes in cell-cell type interactions between experimental conditions. Odds ratios for different subsets of immune cells were plotted using ggplot2.

Intratumoral and systemic cytokine measurements

Serum was collected in EDTA-containing tubes (Sarstedt), and IL-12 levels were determined using the IL-12 p70 Mouse Uncoated ELISA Kit (Invitrogen). Isolated tumors were snap-frozen on dry ice. Before thawing, a 5-mm metal bead and 1 ml of lysis buffer [1:100; 20 mM tris-HCl (pH 7.5), 0.5% Tween 20, 150 mM NaCl, and Sigma-Aldrich protease inhibitors] were added to the tubes. Tumors were lysed using a TissueLyser (QIAGEN) for 5 min at 25 Hz. After centrifugation, protein concentrations were determined with the Pierce BCA Protein Assay Kit (Thermo Fisher Scientific). CCL5 concentration in the tumor lysates was analyzed by ELISA (Mouse RANTES Uncoated ELISA Kit, Invitrogen) and normalized to the determined total protein concentrations.

Patients and sample preparation

Surgical specimens were mechanically dissociated; digested with Accutase (PAA Laboratories), collagenase IV (Worthington), hyaluronidase (MilliporeSigma), and DNAse type I (MilliporeSigma); filtered; washed; and frozen as single-cell suspension for future use. For human ex vivo tumor cultures, surgical specimens were dissected into tumor fragments and frozen for future use. Human peripheral blood mononuclear cells (PBMCs) were isolated by density gradient centrifugation using Histopaque-1077 (MilliporeSigma) from buffy coats obtained from healthy blood donors (Blood Bank, University Hospital Basel). PBMCs were frozen for later use in liquid nitrogen. For NK cell–depleted cocultures, a positive selection using CD56 MicroBeads, an LS column, and a MidiMACS Separator was performed (Miltenyi). Ethics approval was obtained from the local ethical committee to analyze the tissue and blood samples (Ethikkommission Nordwestschweiz), and written informed consent was obtained from all patients before sample collection.

Ex vivo human immune cells and tumor coculture experiments

Healthy donor PBMCs or tumor digest samples, processed as described above, were cocultured with OVCAR3 human ovarian cancer cell line, similarly to as described by Natoli et al. (31). Briefly, 6000 OVCAR3 cells were seeded on the wells of a flat-bottom 96-well plate in RPMI containing L-glutamine (R8758, Sigma-Aldrich), supplemented with penicillin/streptomycin (100 ng/ml; Sigma-Aldrich) and 10% FBS (Sigma-Aldrich). After 2 hours, the medium was replaced with fully supplemented RPMI containing AdV5-huIL12 or empty vector control (AdV5-control) at a PFU of 1000 per cell. Additional control wells were left untreated. After 2 hours of incubation, the medium was replaced to remove the virus, and the tumor cells were incubated for 2 days at 37°C at 5% CO_2. A total of 300,000 healthy donor PBMCs or single cells from tumor digest samples were then added to the wells of the 96-well plate in a final volume of 200 μl per well. Tumor cell (OVCAR3) viability was assessed by an 3-[4,5-dimethylthiazol-2-yl]-2,5 diphenyl tetrazolium bromide (MTT) assay, and flow cytometry was conducted on the suspension cells (PBMCs and TILs) after 3 days of coculture. The supernatant was collected after 6 days of coculture to assess IFN-γ and CCL5 production using a human IFN-γ ELISA set (BD OptEIA, 555142) and an ELISA MAX Deluxe Set Human CCL5 (BioLegend, 440804), respectively, according to the manufacturers' instructions.

Ex vivo tumor fragment culture

Tumor fragment cultures were prepared as described by Voabli et al. (32). Briefly, frozen patient tumor fragments were slowly thawed at 37°C and extensively washed in PBS and warm RPMI containing L-glutamine (R8758, Sigma-Aldrich), supplemented with penicillin/streptomycin (100 ng/ml; Sigma-Aldrich), 10% FBS (Sigma-Aldrich), 1× minimum essential medium nonessential amino acids (Gibco), and 1 mM sodium pyruvate (Sigma-Aldrich).

Single tumor fragments were then embedded in a total of 80 μl of an artificial extracellular matrix within the wells of a flat-bottom 96-well plate. The extracellular matrix was prepared by mixing icecold sodium bicarbonate (1.1% final concentration; Sigma-Aldrich), collagen I (1 mg/ml final concentration; Corning), and fully supplemented RPMI with ice-cold Matrigel (4 mg/ml final concentration; Matrix High Concentration, Phenol Red–Free, BD Biosciences). Forty microliters of matrix was solidified by incubation at 37°C for 20 to 30 min. One tumor fragment per well was placed on top of the presolidified matrix, after which a second layer of 40 μl matrix was added. Plates were then placed in a 37°C incubator for further 20 to 30 min. Fully supplemented RPMI (110 μl) was added on top of the matrix. A total of 1×10^8 PFU of AdV5-huIL12 or control AdV5-control or nivolumab (10 μg/ml of final concentration) was added to each well containing individual tumor fragments. Between 6 and 12 fragments were used for each treatment conditions. After 48 hours of incubation at 37°C, the fragments were pooled and enzymatically digested and filtered into single-cell suspensions, as described above. Flow cytometry was conducted, and the supernatant was collected from each well to assess IFN-γ and CCL5 concentrations using a human IFN-γ ELISA set (BD OptEIA, 555142) and an ELISA MAX Deluxe Set Human CCL5 (BioLegend, 440804), respectively, according to the manufacturers' instructions.

MTT assay

To assess tumor cell viability in coculture experiments, an MTT assay was used as follows. The medium from the coculture wells was removed, and the wells were gently washed once with PBS to remove suspension cells. MTT (Sigma-Aldrich) was then added at 500 μg/ml, and the tumor cells were incubated at 37°C for 2 to 3 hours.

Formazan crystals were resuspended in 90 μl of dimethyl sulfoxide (Sigma-Aldrich), and absorbance was measured at a wavelength of 570 nm.

Bioinformatic analysis of published gene expression data of human melanoma samples

We received the normalized NanoString RNA expression data from the NCT01502293 trial (OncoSec), in which patients received IL-12–encoding mRNA by intratumoral electroporation (*16*). The gene signatures for different immune subpopulations were retrieved from the PanCancer Immunology NanoString panel. The transcripts within the "Cytotoxic cells" signature cannot be attributed to a single-cell type and are found in other signature lists of both NK and CD8 T cells. Therefore, its transcripts were merged with the cytotoxic NK and CD8 T cells resulting in the "CD8+ T cells" and "NK cells" signatures. Neither "CD8+ T cells" nor "NK cells" contained the *CCL5* transcript. Downstream analysis of all NanoString data was performed using R version 4.0.2 and visualized in Graph-Pad Prism 9.

Immune cell infiltration was estimated by calculating a signature score as described by Cursons *et al.* (*78*). Briefly, all transcripts for each sample were ordered by decreasing expression, and the signature score was defined as

$$1 - \frac{\text{mean rank of signature transcripts}}{\text{number of all transcripts}}$$

Thus, a high signature score indicates the enrichment of signature transcripts among genes with high expression. To find genes that correlate with the NK cells signature score, we performed a linear regression for signature scores with log-transformed transcript counts. *P* values were adjusted by the Benjamini-Hochberg correction method.

We also reanalyzed RNAseq data of samples from patients with tumors treated with anti–PD-1 antibodies (nivolumab) (*36*). Data were downloaded from the Gene Expression Omnibus (GEO) under accession number GSE91061. Only patients with both pre- and post-treatment samples and evaluated responses were analyzed. Counts were normalized by library size using edgeR and displayed as log counts per million using GraphPad Prism 9. Paired two-way analysis of variance (ANOVA) with multiple comparisons and post hoc test were used to calculate significances for increased *CCL5* expression upon treatment in clinical benefit (CB). The availability of RNAseq data allowed the use of more complex gene signatures than with NanoString data above. Therefore, we used the signatures described by Tirosh *et al.* and Cursons *et al.* for this analysis (*78, 79*). Because we wanted to correlate signatures with *CCL5* expression, *CCL5* was excluded from the T cell signature provided by Tirosh *et al.* (*79*). Signature scores were calculated as described above.

For the reanalysis of Zillionis *et al.* (*33*) scRNAseq dataset, we downloaded the precleaned count matrix from GEO under accession number GSE127465. The dataset was analyzed using the Bioconductor packages SingleCellExperiment and scater. PCA was performed using the top 4000 variable gene log counts. UMAP dimension reduction was performed on the PCA values using the scater runUMAP with 15 neighbors. *CCL5* expression per cell was visualized by ggplot2 using UMAP coordinates. To construct the NK1 and NK2 signatures, we extracted the *z* scores for genes enriched in either cluster using the online tool of the original publication. We then selected genes with a *z* score of >0.5 and a minimum difference in *z* score between the two subsets of 0.5.

We also obtained signatures for tissue-resident NK cells from Marquardt *et al.* and a signature for CD56^bright CD16^neg NK cells from Hanna *et al.* (*34, 35*). A score for each signature as above was then calculated for each cell in the Zilionis dataset. Violin plots of these values were then plotted using GraphPad Prism.

Similarly, we also obtained the scRNAseq dataset described by Sade-Feldmann (*37*) under GEO accession number GSE120575. As described in their original publication, genes were filtered for protein coding genes and minimum expression of >4.5 log counts in at least 10 cells. Cells were filtered to have >2.5 mean log counts of their listed housekeeping genes. Cells with a high fraction mitochondrial reads (>3 SDs; dying cells) and very many detected genes (>4 SDs; doublets) were excluded. PCA and UMAP dimension reductions were calculated as above. Clustering was performed using buildSNNGraphs of the scran package from PCA values and *k* = 15. Cluster 8 consisted of NK cells on the basis of its high expression of *NCR1*, *NCAM*, and *FCGR3A*. For each cell in this NK cluster, we calculated the mean score for NK1 and NK2 signatures as described above. Then, we summarized the mean NK1 and NK2 value for the NK cells of each patient. The values for responding and nonresponding patients were then visualized as a ratio between NK2 and NK1 cells using GraphPad Prism.

Statistical analysis

For normally distributed datasets, we used two-tailed Student's *t* test and one-way ANOVA followed by Holm-Sidak multiple comparison test. When variables were not normally distributed, we performed nonparametric Mann-Whitney or Kruskal-Wallis tests. For survival analysis, *P* values were computed using the log rank test. Two-way ANOVA was used to compare tumor growth curves and grouped datasets. *P* values > 0.05 were considered not significant, and *P* values < 0.05 were considered significant. *$P < 0.05$, **$P < 0.01$, ***$P < 0.001$, and ****$P < 0.0001$.

SUPPLEMENTARY MATERIALS

www.science.org/doi/10.1126/scitranslmed.abm9043
Figs. S1 to S9
Tables S1 and S2
Data file S1
MDAR Reproducibility Checklist

View/request a protocol for this paper from *Bio-protocol*.

REFERENCES AND NOTES

1. A. D. Waldman, J. M. Fritz, M. J. Lenardo, A guide to cancer immunotherapy: From T cell basic science to clinical practice. *Nat. Rev. Immunol.* **20**, 651–668 (2020).
2. K. C. Barry, J. Hsu, M. L. Broz, F. J. Cueto, M. Binnewies, A. J. Combes, A. E. Nelson, K. Loo, R. Kumar, M. D. Rosenblum, M. D. Alvarado, D. M. Wolf, D. Bogunovic, N. Bhardwaj, A. I. Daud, P. K. Ha, W. R. Ryan, J. L. Pollack, B. Samad, S. Asthana, V. Chan, M. F. Krummel, A natural killer–dendritic cell axis defines checkpoint therapy—Responsive tumor microenvironments. *Nat. Med.* **24**, 1178–1191 (2018).
3. A. Gardner, Á. de M. Pulido, B. Ruffell, Dendritic cells and their role in immunotherapy. *Front. Immunol.* **11**, 924 (2020).
4. N. D. Huntington, J. Cursons, J. Rautela, The cancer–natural killer cell immunity cycle. *Nat. Rev. Cancer* **20**, 437–454 (2020).
5. C. S. Garris, S. P. Arlauckas, R. H. Kohler, M. P. Trefny, S. Garren, C. Piot, C. Engblom, C. Pfirschke, M. Siwicki, J. Gungabeesoon, G. J. Freeman, S. E. Warren, S. F. Ong, E. Browning, C. G. Twitty, R. H. Pierce, M. H. Le, A. P. Algazi, A. I. Daud, S. I. Pai, A. Zippelius, R. Weissleder, M. J. Pittet, Successful anti–PD-1 cancer immunotherapy requires t cell-dendritic cell crosstalk involving the cytokines IFN-γ and IL-12. *Immunity* **49**, 1148–1161.e7 (2018).
6. S. Tugues, S. H. Burkhard, I. Ohs, M. Vrohlings, K. Nussbaum, J. Vom Berg, P. Kulig, B. Becher, New insights into IL-12-mediated tumor suppression. *Cell Death Differ.* **22**, 237–246 (2015).

7. B. Ruffell, D. Chang-Strachan, V. Chan, A. Rosenbusch, C. M. T. Ho, N. Pryer, D. Daniel, E. S. Hwang, H. S. Rugo, L. M. Coussens, Macrophage IL-10 blocks CD8⁺ T cell-dependent responses to chemotherapy by suppressing IL-12 expression in intratumoral dendritic cells. *Cancer Cell* **26**, 623–637 (2014).

8. M. Ayers, J. Lunceford, M. Nebozhyn, E. Murphy, A. Loboda, D. R. Kaufman, A. Albright, J. D. Cheng, S. P. Kang, V. Shankaran, S. A. Piha-Paul, J. Yearley, T. Y. Seiwert, A. Ribas, T. K. McClanahan, IFN-γ-related mRNA profile predicts clinical response to PD-1 blockade. *J. Clin. Invest.* **127**, 2930–2940 (2017).

9. J. P. Böttcher, E. Bonavita, P. Chakravarty, H. Blees, M. Cabeza-Cabrerizo, S. Sammicheli, N. C. Rogers, E. Sahai, S. Zelenay, C. R. e Sousa, NK cells stimulate recruitment of cDC1 into the tumor microenvironment promoting cancer immune control. *Cell* **172**, 1022–1037.e14 (2018).

10. J. Cursons, A gene signature predicting natural killer cell infiltration and improved survival in melanoma patients. *Cancer Immunol. Res.* **7**, 1162–1174 (2019).

11. Y. Zhao, C. K. Lee, C. H. Lin, R. B. Gassen, X. Xu, Z. Huang, C. Xiao, C. Bonorino, L. F. Lu, J. D. Bui, E. Hui, PD-L1:CD80 cis-heterodimer triggers the co-stimulatory receptor CD28 while repressing the inhibitory PD-1 and CTLA-4 pathways. *Immunity* **51**, 1059–1073.e9 (2019).

12. H. Lee, Integrated molecular and immunophenotypic analysis of NK cells in anti-PD-1 treated metastatic melanoma patients. *Onco. Targets. Ther.* **8**, e1537581 (2019).

13. G. R. Weiss, M. A. O'Donnell, K. Loughlin, K. Zonno, R. J. Laliberte, M. L. Sherman, Phase 1 study of the intravesical administration of recombinant human interleukin-12 in patients with recurrent superficial transitional cell carcinoma of the bladder. *J. Immunother.* **26**, 343–348 (2003).

14. J. A. Hurteau, J. A. Blessing, S. L. DeCesare, W. T. Creasman, Evaluation of recombinant human interleukin-12 in patients with recurrent or refractory ovarian cancer: A gynecologic oncology group study. *Gynecol. Oncol.* **82**, 7–10 (2001).

15. K. G. Nguyen, M. R. Vrabel, S. M. Mantooth, J. J. Hopkins, E. S. Wagner, T. A. Gabaldon, D. A. Zaharoff, Localized interleukin-12 for cancer immunotherapy. *Front. Immunol.* **11**, 1–36 (2020).

16. A. Algazi, S. Bhatia, S. Agarwala, M. Molina, K. Lewis, M. Faries, L. Fong, L. P. Levine, M. Franco, A. Oglesby, C. Ballesteros-Merino, C. B. Bifulco, B. A. Fox, D. Bannavong, R. Talia, E. Browning, M. H. Le, R. H. Pierce, S. Gargosky, K. K. Tsai, C. Twitty, A. I. Daud, Intratumoral delivery of tavokinogene telseplasmid yields systemic immune responses in metastatic melanoma patients. *Ann. Oncol.* **31**, 532–540 (2019).

17. J. Strauss, C. R. Heery, J. W. Kim, C. Jochems, R. N. Donahue, A. S. Montgomery, S. McMahon, E. Lamping, J. L. Marte, R. A. Madan, M. Bilusic, M. R. Silver, E. Bertotti, J. Schlom, J. L. Gulley, First-in-human phase I trial of a tumor-targeted cytokine (NHS-IL12) in subjects with metastatic solid tumors. *Clin. Cancer Res.* **25**, 99–109 (2019).

18. B. Sangro, G. Mazzolini, J. Ruiz, M. Herraiz, J. Quiroga, I. Herrero, A. Benito, J. Larrache, J. Pueyo, J. C. Subtil, C. Olagüe, J. Sola, B. Sádaba, C. Lacasa, I. Melero, C. Qian, J. Prieto, Phase I trial of intratumoral injection of an adenovirus encoding interleukin-12 for advanced digestive tumors. *J. Clin. Oncol.* **22**, 1389–1397 (2004).

19. O. Hamid, M. Hellman, B. Carneiro, T. Marron, V. Subbiah, I. Mehmi, J. Eyles, V. Dubois, B. Ridgway, O. Hamid, A. G. Hernandez, 19O preliminary safety, antitumor activity and pharmacodynamics results of HIT-IT MEDI1191 (mRNA IL-12) in patients with advanced solid tumours and superficial lesions. *Ann. Oncol.* **32**, S9 (2021).

20. S. N. Smith, R. Schubert, B. Simic, D. Brücher, M. Schmid, N. Kirk, P. C. Freitag, V. Gradinaru, A. Plückthun, The SHREAD gene therapy platform for paracrine delivery improves tumor localization and 3 intratumoral effects of a clinical antibody. *Proc. Natl. Acad. Sci. U.S.A.* **118**, e2017925118 (2021).

21. D. Brücher, N. Kirchhammer, S. N. Smith, J. Schumacher, N. Schumacher, J. Kolibius, P. C. Freitag, M. Schmid, F. Weiss, C. Keller, M. Grove, U. F. Greber, A. Zippelius, A. Plückthun, iMATCH: An integrated modular assembly system for therapeutic combination high-capacity adenovirus gene therapy. *Mol. Ther. Methods Clin. Dev.* **20**, 572–586 (2021).

22. M. Schmid, P. Ernst, A. Honegger, M. Suomalainen, M. Zimmermann, L. Braun, S. Stauffer, C. Thom, B. Dreier, M. Eibauer, A. Kipar, V. Vogel, U. F. Greber, O. Medalia, A. Plückthun, Adenoviral vector with shield and adapter increases tumor specificity and escapes liver and immune control. *Nat. Commun.* **9**, 450 (2018).

23. Y. Goltsev, N. Samusik, J. Kennedy-Darling, S. Bhate, M. Hale, G. Vazquez, S. Black, G. P. Nolan, Deep profiling of mouse splenic architecture with CODEX multiplexed imaging. *Cell* **174**, 968–981.e15 (2018).

24. M. A. Morris, D. R. Gibb, F. Picard, V. Brinkmann, M. Straume, K. Ley, Transient T cell accumulation in lymph nodes and sustained lymphopenia in mice treated with FTY720. *Eur. J. Immunol.* **35**, 3570–3580 (2005).

25. L. F. De Andrade, Y. Lu, A. Luoma, Y. Ito, D. Pan, J. W. Pyrdol, C. H. Yoon, G. C. Yuan, K. W. Wucherpfennig, Discovery of specialized NK cell populations infiltrating human melanoma metastases. *JCI Insight* **4**, e133103 (2019).

26. D. Brownlie, M. Scharenberg, J. E. Mold, J. Hard, E. Kekalainen, M. Buggert, S. Nguyen, J. N. Wilson, M. Al-Ameri, H. G. Ljunggren, N. Marquardt, J. Michaelsson, Expansions of adaptive-like NK cells with a tissue-resident phenotype in human lung and blood. *Proc. Natl. Acad. Sci. U.S.A.* **118**, e2016580118 (2021).

27. A. Crinier, P. Milpied, B. Escalière, C. Piperoglou, J. Galluso, A. Balsamo, L. Spinelli, I. Cervera-Marzal, M. Ebbo, M. Girard-Madoux, S. Jaeger, E. Bollon, S. Hamed, J. Hardwigsen, S. Ugolini, F. Vély, E. Narni-Mancinelli, E. Vivier, High-dimensional single-cell analysis identifies organ-specific signatures and conserved NK cell subsets in humans and mice. *Immunity* **49**, 971–986.e5 (2018).

28. L. Chiossone, J. Chaix, N. Fuseri, C. Roth, E. Vivier, T. Walzer, Maturation of mouse NK cells is a 4-stage developmental program. *Blood* **113**, 5488–5496 (2009).

29. E. Hashemi, S. Malarkannan, Tissue-resident NK cells: Development, maturation, and clinical relevance. *Cancer* **12**, 1–23 (2020).

30. K. Hildner, B. T. Edelson, W. E. Purtha, M. Diamond, H. Matsushita, M. Kohyama, B. Calderon, B. U. Schraml, E. R. Unanue, M. S. Diamond, R. D. Schreiber, T. L. Murphy, K. M. Murphy, Batf3 deficiency reveals a critical role for CD8α⁺ dendritic cells in cytotoxic T cell immunity. *Science* **322**, 1097–1100 (2008).

31. M. Natoli, N. Bonito, J. D. Robinson, S. Ghaem-Maghami, Y. Mao, Human ovarian cancer intrinsic mechanisms regulate lymphocyte activation in response to immune checkpoint blockade. *Cancer Immunol. Immunother.* **69**, 1391–1401 (2020).

32. P. Voabil, M. de Bruijn, L. Roelofsen, S. Hendriks, S. Brokamp, M. van den Braber, A. Broeks, J. Sanders, P. Herzig, A. Zippelius, C. Blank, K. Hartemink, K. Monkhorst, J. Haanen, T. Schumacher, D. Thommen, An ex vivo tumor fragment platform to dissect response to PD-1 blockade in cancer. *Nat. Med.* **27**, 1250–1261 (2021).

33. R. Zilionis, C. Engblom, C. Pfirschke, V. Savova, D. Zemmour, H. D. Saatcioglu, I. Krishnan, G. Maroni, C. V. Meyerovitz, C. M. Kerwin, S. Choi, W. G. Richards, A. De Rienzo, D. G. Tenen, R. Bueno, E. Levantini, M. J. Pittet, A. M. Klein, Single-cell transcriptomics of human and mouse lung cancers reveals conserved myeloid populations across individuals and species. *Immunity* **50**, 1317–1334.e10 (2019).

34. J. Hanna, P. Bechtel, Y. Zhai, F. Youssef, K. McLachlan, O. Mandelboim, Novel insights on human NK cells' immunological modalities revealed by gene expression profiling. *J. Immunol.* **173**, 6547–6563 (2004).

35. N. Marquardt, E. Kekäläinen, P. Chen, M. Lourda, J. N. Wilson, M. Scharenberg, P. Bergman, M. Al-Ameri, J. Hård, J. E. Mold, H. G. Ljunggren, J. Michaëlsson, Unique transcriptional and protein-expression signature in human lung tissue-resident NK cells. *Nat. Commun.* **10**, 1–12 (2019).

36. N. Riaz, J. J. Havel, V. Makarov, A. Desrichard, W. J. Urba, J. S. Sims, F. S. Hodi, S. Martín-Algarra, R. Mandal, W. H. Sharfman, S. Bhatia, W. J. Hwu, T. F. Gajewski, C. L. Slingluff Jr., D. Chowell, S. M. Kendall, R. Chang, R. Shah, F. Kuo, L. G. T. Morris, J. W. Sidhom, J. P. Schneck, C. E. Horak, N. Weinhold, T. A. Chan, Tumor and microenvironment evolution during immunotherapy with nivolumab. *Cell* **171**, 934–949.e15 (2017).

37. M. Sade-Feldman, Defining T cell states associated with response to checkpoint immunotherapy in melanoma. *Cell* **175**, 998–1013.e20 (2018).

38. R. B. Mokhtari, T. S. Homayouni, N. Baluch, E. Morgatskaya, S. Kumar, B. Das, H. Yeger, Combination therapy in combating cancer. *Oncotarget* **8**, 38022–38043 (2017).

39. J. Sun, Q. Wei, Y. Zhou, J. Wang, Q. Liu, H. Xu, A systematic analysis of FDA-approved anticancer drugs. *BMC Syst. Biol.* **11**, 87 (2017).

40. F. Meric-Bernstam, J. Larkin, J. Tabernero, C. Bonini, Enhancing anti-tumour efficacy with immunotherapy combinations. *Lancet* **397**, 1010–1022 (2020).

41. A. P. Algazi, C. G. Twitty, K. K. Tsai, M. Le, R. Pierce, E. Browning, R. Hermiz, D. A. Canton, D. Bannavong, A. Oglesby, M. Francisco, L. Fong, M. J. Pittet, S. P. Arlauckas, C. Garris, L. P. Levine, C. Bifulco, C. Ballesteros-Merino, S. Bhatia, S. Gargosky, R. H. I. Andtbacka, B. A. Fox, M. D. Rosenblum, A. I. Daud, Phase II trial of IL-12 plasmid transfection and PD-1 blockade in immunologically quiescent melanoma. *Clin. Cancer Res.* **26**, 2827–2837 (2020).

42. R. S. Riley, C. H. June, R. Langer, M. J. Mitchell, Delivery technologies for cancer immunotherapy. *Nat. Rev. Drug Discov.* **18**, 175–196 (2019).

43. B. Dreier, A. Honegger, C. Hess, G. Nagy-Davidescu, P. R. E. Mittl, M. G. Grütter, N. Belousova, G. Mikheeva, V. Krasnykh, A. Plückthun, Development of a generic adenovirus delivery system based on structure-guided design of bispecific trimeric DARPin adapters. *Proc. Natl. Acad. Sci. U.S.A.* **110**, E869–E877 (2013).

44. B. Dreier, A. Plückthun, Rapid selection of high-affinity binders using ribosome display. *Methods Mol. Biol.* **805**, 261–286 (2012).

45. A. Plückthun, Designed ankyrin repeat proteins (DARPins): Binding proteins for research, diagnostics, and therapy. *Annu. Rev. Pharmacol. Toxicol.* **55**, 489–511 (2015).

46. M. Yan, B. A. Parker, R. Schwab, R. Kurzrock, HER2 aberrations in cancer: Implications for therapy. *Cancer Treat. Rev.* **40**, 770–780 (2014).

47. S. Kakarla, X. T. Song, S. Gottschalk, Cancer-associated fibroblasts as targets for immunotherapy. *Immunotherapy* **4**, 1129–1138 (2012).

48. M. Trüb, F. Uhlenbrock, C. Claus, P. Herzig, V. Karanikas, M. Bacac, M. Amann, R. Albrecht, C. Ferrara-Koller, D. Thommen, S. Rothschield, S. Savic, K. D. Mertz, G. Cathomas, R. Rosenberg, V. Heinzelmann-Schwarz, M. Wiese, D. Lardinois, P. Umana, C. Klein, H. Laubli, A. S. Kashyap, A. Zippelius, Fibroblast activation protein-targeted-4-1BB ligand agonist amplifies effector functions of intratumoral T cells in human cancer. *J. Immunother. Cancer* **8**, e000238 (2020).

49. D. Muruve, V. Pétrilli, A. Zaiss, L. White, S. A. Clark, P. J. Ross, R. J. Parks, J. Tschopp, The inflammasome recognizes cytosolic microbial and host DNA and triggers an innate immune response. *Nature* **452**, 103–107 (2008).

Kirchhammer *et al.*, *Sci. Transl. Med.* **14**, eabm9043 (2022)   13 July 2022

16 of 17

50. D. M. Appledorn, S. Patial, S. Godbehere, N. Parameswaran, A. Amalfitano, TRIF, and TRIF-interacting TLRs differentially modulate several adenovirus vector-induced immune responses. *J. Innate Immun.* **1**, 376–388 (2009).

51. D. M. Appledorn, S. Patial, A. M. Bride, S. Godbehere, N. Van Rooijen, N. Parameswaran, A. Amalfitano, Adenovirus vector-induced innate inflammatory mediators, MAPK signaling, as well as adaptive immune responses are dependent upon both TLR2 and TLR9 in vivo. *J. Immunol.* **181**, 2134–2144 (2008).

52. Z. Urban-Wojciuk, M. M. Khan, B. L. Oyler, R. Fåhraeus, N. Marek-Trzonkowska, A. Nita-Lazar, T. R. Hupp, D. R. Goodlett, The role of tlrs in anti-cancer immunity and tumor rejection. *Front. Immunol.* **10**, 2388 (2019).

53. M. Budhwani, R. Mazzieri, R. Dolcetti, Plasticity of type I interferon-mediated responses in cancer therapy: From anti-tumor immunity to resistance. *Front. Oncol.* **8**, 322 (2018).

54. R. Saleh, E. Elkord, Acquired resistance to cancer immunotherapy: Role of tumor-mediated immunosuppression. *Semin. Cancer Biol.* **65**, 13–27 (2020).

55. S. Spranger, D. Dai, B. Horton, T. F. Gajewski, Tumor-residing Batf3 dendritic cells are required for effector t cell trafficking and adoptive t cell therapy. *Cancer Cell* **31**, 711–723.e4 (2017).

56. C. Degos, M. Heinemann, J. Barrou, N. Boucherit, E. Lambaudie, A. Savina, L. Gorvel, D. Olive, Endometrial tumor microenvironment alters human NK cell recruitment, and resident NK cell phenotype and function. *Front. Immunol.* **10**, 877 (2019).

57. L. Ducimetière, G. Lucchiari, G. Litscher, M. Nater, L. Heeb, N. G. Nuñez, L. Wyss, D. Burri, M. Vermeer, J. Gschwend, A. E. Moor, B. Becker, M. van den Broek, S. Tugues, Conventional NK cells and tissue-resident ILC1s join forces to control liver metastasis. *Proc. Natl. Acad. Sci. U.S.A.* **118**, e2026271118 (2021).

58. H. Sun, L. Liu, Q. Huang, H. Liu, M. Huang, J. Wang, H. Wen, R. Lin, K. Qu, K. Li, H. Wei, W. Xiao, R. Sun, Z. Tian, C. Sun, Accumulation of tumor-infiltrating CD49a$^+$ NK cells correlates with poor prognosis for human hepatocellular carcinoma. *Cancer Immunol. Res.* **7**, 1535–1546 (2019).

59. T. T. Murooka, R. Rahbar, E. N. Fish, CCL5 promotes proliferation of MCF-7 cells through mTOR-dependent mRNA translation. *Biochem. Biophys. Res. Commun.* **387**, 381–386 (2009).

60. N. Casagrande, C. Borghese, L. Visser, M. Mongiat, A. Colombatti, D. Aldinucci, CCR5 antagonism by maraviroc inhibits hodgkin lymphoma microenvironment interactions and xenograft growth. *Haematologica* **104**, 564–575 (2019).

61. A. E. Karnoub, A. B. Dash, A. P. Vo, A. Sullivan, M. W. Brooks, G. W. Bell, A. L. Richardson, K. Polyak, R. Tubo, R. A. Weinberg, Mesenchymal stem cells within tumour stroma promote breast cancer metastasis. *Nature* **449**, 557–563 (2007).

62. X. Jiao, M. A. Velasco-Velazquez, M. Wang, Z. Li, H. Rui, A. R. Peck, J. E. Korkola, X. Chen, S. Xu, J. B. DuHadaway, S. Guerrero-Rodriguez, S. Addya, D. Sicoli, Z. Mu, G. Zhang, A. Stucky, X. Zhang, M. Cristofanilli, A. Fatatis, J. W. Gray, J. F. Zhong, G. C. Prendergast, R. G. Pestell, CCR5 governs DNA damage repair and breast cancer stem cell expansion. *Cancer Res.* **78**, 1657–1671 (2018).

63. P. Debré, B. Combadiere, A. Boissonnas, O. Bonduelle, M. Maho, E. Lavergne, C. Combadière, M. Iga, Increases tumor cell infiltration overexpression delays tumor growth and intratumoral CC chemokine ligand 5. *J. Immunol.* **173**, 3755–3762 (2021).

64. D. Dangaj, M. Bruand, A. J. Grimm, C. Ronet, D. Barras, P. A. Duttagupta, E. Lanitis, J. Duraiswamy, J. L. Tanyi, F. Benencia, J. Conejo-Garcia, H. R. Ramay, K. T. Montone, D. J. Powell, P. A. Gimotty, A. Facciabene, D. G. Jackson, J. S. Weber, S. J. Rodig, S. F. Hodi, L. E. Kandalaft, M. Irving, L. Zhang, P. Foukas, S. Rusakiewicz, M. Delorenzi, G. Coukos, Cooperation between constitutive and inducible chemokines enables T cell engraftment and immune attack in solid tumors. *Cancer Cell* **35**, 885–900.e10 (2019).

65. J. M. Romero, B. T. Grünwald, G.-H. Jang, P. P. Bavi, A. Jhaveri, M. Masoomian, S. E. Fischer, A. Zhang, R. E. Denroche, I. M. Lungu, A. De Luca, J. M. S. Bartlett, J. Xu, N. Li, S. Dhaliwal, S.-B. Liang, D. Chadwick, F. Vyas, P. Bronsert, R. Khokha, T. L. McGaha, F. Notta, P. S. Ohashi, S. J. Done, G. M. O'Kane, J. M. Wilson, J. J. Knox, A. Connor, Y. Wang, G. Zogopoulos, S. Gallinger, A four-chemokine signature is associated with a T cell-inflamed phenotype in primary and metastatic pancreatic cancer. *Clin. Cancer Res.* **26**, 1997–2010 (2020).

66. N. Jacquelot, C. Seillet, E. Vivier, G. T. Belz, Innate lymphoid cells and cancer. *Nat. Immunol.* **23**, 371–379 (2022).

67. J. Luo, Z. L. Deng, X. Luo, N. Tang, W. X. Song, J. Chen, K. A. Sharff, H. H. Luu, R. C. Haydon, K. W. Kinzler, B. Vogelstein, T. C. He, A protocol for rapid generation of recombinant adenoviruses using the AdEasy system. *Nat. Protoc.* **2**, 1236–1247 (2007).

68. L. D'Amico, U. Menzel, M. Prummer, P. Müller, M. Buchi, A. Kashyap, U. Haessler, A. Yermanos, R. Gébleux, M. Briendl, T. Hell, F. I. Wolter, R. R. Beerli, I. Truxova, Š. Radek, T. Vlajnic, U. Grawunder, S. Reddy, A. Zippelius, A novel anti-HER2 anthracycline-based antibody-drug conjugate induces adaptive anti-tumor immunity and potentiates PD-1 blockade in breast cancer. *J. Immunother. Cancer* **7**, 16 (2018).

69. flowCore: FlowCore: Basic structures for flow cytometry data version 2.2.0 from Bioconductor; https://rdrr.io/bioc/flowCore/.

70. CATALYST: Cytometry dATa anALYSis Tools version 1.14.0 from Bioconductor; https://rdrr.io/bioc/CATALYST/.

71. GitHub, JinmiaoChenLab/Rphenograph: Rphenograph: R implementation of the PhenoGraph algorithm; https://github.com/JinmiaoChenLab/Rphenograph.

72. J. H. Levine, E. F. Simonds, S. C. Bendall, K. L. Davis, E. A. D. Amir, M. D. Tadmor, O. Litvin, H. G. Fienberg, A. Jager, E. R. Zunder, R. Finck, A. L. Gedman, I. Radtke, J. R. Downing, D. Pe'er, G. P. Nolan, Data-driven phenotypic dissection of AML reveals progenitor-like cells that correlate with prognosis. *Cell* **162**, 184–197 (2015).

73. CRAN, Package pheatmap; https://cran.r-project.org/web/packages/pheatmap/index.html.

74. GitHub, BIOP/ijp-kheops; https://github.com/BIOP/ijp-kheops.

75. GitHub, stardist/stardist: StarDist—Object detection with star-convex shapes; https://github.com/stardist/stardist.

76. P. Bankhead, M. B. Loughrey, J. A. Fernández, Y. Dombrowski, D. G. McArt, P. D. Dunne, S. McQuaid, R. T. Gray, L. J. Murray, H. G. Coleman, J. A. James, M. Salto-Tellez, P. W. Hamilton, QuPath: Open source software for digital pathology image analysis. *Sci. Rep.* **7**, 1–7 (2017).

77. N. Samusik, Z. Good, M. H. Spitzer, K. L. Davis, G. P. Nolan, Automated mapping of phenotype space with single-cell data. *Nat. Methods* **13**, 493–496 (2016).

78. J. Cursons, F. Souza-Fonseca-Guimaraes, M. Foroutan, A. Anderson, F. Hollande, S. Hediyeh-Zadeh, A. Behren, N. D. Huntington, M. J. Davis, A gene signature predicting natural killer cell infiltration and improved survival in melanoma patients. *Cancer Immunol. Res.* **7**, 1162–1174 (2019).

79. I. Tirosh, B. Izar, S. M. Prakadan, M. H. Wadsworth, D. Treacy, J. J. Trombetta, A. Rotem, C. Rodman, C. Lian, G. Murphy, M. Fallahi-Sichani, K. Dutton-Regester, J. R. Lin, O. Cohen, P. Shah, D. Lu, A. S. Genshaft, T. K. Hughes, C. G. K. Ziegler, S. W. Kazer, A. Gaillard, K. E. Kolb, A. C. Villani, C. M. Johannessen, A. Y. Andreev, E. M. Van Allen, M. Bertagnolli, P. K. Sorger, R. J. Sullivan, K. T. Flaherty, D. T. Frederick, J. Jané-Valbuena, C. H. Yoon, O. Rozenblatt-Rosen, A. K. Shalek, A. Regev, L. A. Garraway, Dissecting the multicellular ecosystem of metastatic melanoma by single-cell RNA-seq. *Science* **352**, 189–196 (2016).

Kirchhammer *et al.*, *Sci. Transl. Med.* **14**, eabm9043 (2022)   13 July 2022

17 of 17

Science Translational Medicine

NK cells with tissue-resident traits shape response to immunotherapy by inducing adaptive antitumor immunity

Nicole KirchhammerMarcel P. TrefnyMarina NatoliDominik BrücherSheena N. SmithFranziska WernerVictoria KochDavid SchreinerEwelina BartoszekMélanie BuchiMarkus SchmidDaniel BreuK. Patricia HartmannPolina ZaytsevaDaniela S. ThommenHeinz LäubliJan P. BöttcherMichal A. StanczakAbhishek S. KashyapAndreas PlückthunAlfred Zippelius

Improving IL-12 immunotherapy

Interleukin-12 (IL-12) has been a successful form of cancer immunotherapy in preclinical studies, but its translation has been lacking in early patient clinical trials. To investigate this dichotomy, Kirchhammer *et al.* used an adenovirus platform to treat patient-derived xenografts intratumorally with IL-12 immunotherapy. They saw that the efficacy of IL-12 treatment was dependent on a population of tissue-associated natural killer (NK) cells that produced the chemoattractant CCL5. They saw that treatment failure could be overcome with an intratumoral delivery of CCL5, suggesting that a potential combination treatment could be useful in patients and warrants further study.

View the article online
https://www.science.org/doi/10.1126/scitranslmed.abm9043
Permissions
https://www.science.org/help/reprints-and-permissions